

Improving Particle Mesh Accuracy with Analytical Solutions for Newtonian and Modified Newtonian Dynamics

by

Martin Vingerhoets

to obtain the degree of Bachelor of Science
at the Delft University of Technology,
to be defended publicly on Thursday July 4, 2024 at 14:30.

Student number: 5461677
Project duration: Februari 12, 2024 – July 4, 2024
Thesis committee: Dr. P.M. Visser supervisor
Dr. S.W.H. Eijt supervisor
Prof. Dr. J.M. Thijssen
Dr. J.G. Spandaw

An electronic version of this thesis is available at <http://repository.tudelft.nl/>.

Abstract

This paper aims to improve the Particle Mesh (PM) method for Newtonian Dynamics (ND) and Modified Newtonian Dynamics (MOND). The PM method involves discretizing the mass density on a grid using Gaussian smoothing, which is used to calculate the gravitational potential using Fast Fourier Transforms (FFTs). A major downside of Gaussian smoothing is that the mass density of two particles overlaps whenever they are in close proximity, which leads to incorrect orbital dynamics. Hence, the linearity of ND is used to correct the accelerations of particles whenever this overlap in mass density occurs. These short-range corrections involve the use of analytical expressions to eliminate the inaccurate influence of the PM method, correcting the interactions between particle pairs to direct particle-particle interactions. These corrections can introduce instabilities whenever two particles are too close in proximity and the time steps are too large. This issue is mitigated by using a softening parameter in the corrections. In MOND, the linearity in the accelerations is removed, which means that these short-range corrections cannot always be used. They may only be used in the limit of high accelerations, for which MOND reduces to ND. The short-range corrections are tested for circular and elliptical two-body systems, showing a significant reduction in error of their expected orbital trajectories. To test the limitations of the PM method under non-linear accelerations in MOND where no corrections may be applied, a wide binary system is used to determine the minimum distance between particles that still yields somewhat accurate. This also demonstrates that without the use of short-range corrections large grids are required, highlighting a major inefficiency of PM methods. Lastly, the corrections are tested in both ND and MOND using the Plummer and Miyamoto-Nagai models, which represent a sphere and a disk, respectively. The Plummer model showed significant improvements in stability in both ND and MOND. However, the Miyamoto-Nagai model shows less optimistic results in MOND due to the difficulty in placing the particles at a minimum separating particles whenever the accelerations are non-linear. Overall, careful use of these short-range corrections allows for significant improvements in the PM method for both ND and MOND. Further research into optimizing the computational performance of FFTs and short-range corrections using tree codes is still available. Additionally, a time-adaptive PM can be implemented to prevent possible instabilities due to large time steps when using the corrections.

Contents

1	Introduction	1
2	Theory	5
2.1	Newtonian Dynamics	5
2.1.1	Analytical solutions	9
2.1.2	Newtonian Lagrangian	10
2.2	Modified Newtonian Dynamics.	11
2.2.1	Choosing an interpolation function.	11
2.2.2	MOND Lagrangian	12
2.2.3	Analytical solutions	13
2.2.4	MOND variations	15
3	Particle Mesh	17
3.1	Particle-Mesh for Newtonian Dynamics	17
3.1.1	Calculating the Newtonian potential and gravitational field.	19
3.1.2	Interpolating back to original particle locations	21
3.1.3	Time iterations	22
3.1.4	Short-range Newtonian correction.	23
3.2	Calculating the MOND gravitational potential and field	24
4	Galaxy modelling	25
4.1	Galaxy models	25
4.2	Sampling particle locations.	26
4.2.1	Inverse transform sampling	26
4.2.2	Multivariate sampling	27
4.2.3	Rejection sampling	27
4.3	Rotation curves	27
5	Testing	29
5.1	Newtonian particle mesh	29
5.1.1	Mass placement	29
5.1.2	Gravitational potential and field	30
5.1.3	Short-range corrections	32
5.2	MOND particle mesh	37
5.3	Galactic simulations	41
5.3.1	Probabilistic sampling	41
5.3.2	Plummer model.	41
5.3.3	Miyamoto-Nagai model.	45
6	Conclusions and Research Recommendations	47
6.1	Conclusions.	47
6.2	Research recommendations	48

1

Introduction

Over the centuries, our understanding of the cosmos has evolved significantly. Aristotle's theories, which dominated for over a thousand years, distinguished between the behaviors of terrestrial and celestial objects. In the 2nd century CE, Ptolemy's geocentric model, placing Earth at the universe's center, was widely accepted during the Middle Ages. The Renaissance introduced groundbreaking concepts, with Copernicus advocating for a heliocentric model in the 1500s. In the 17th century, Galileo and Kepler made crucial contributions: Galileo's telescope observations showed that the same physical laws apply to both Earth and the cosmos, while Kepler discovered that planets move in elliptical orbits. Christiaan Huygens made significant advancements in understanding inertia, gravitation, and circular motion, developing the concept of centrifugal force and studying the dynamics of moving bodies, further refining the mechanics of planetary motion. In the late 1600s, Isaac Newton combined these ideas with his laws of motion and universal gravitation, forming the foundation of physics for the next three centuries.

Newton's theory is based on three fundamental ideas:

1. An object at rest will stay at rest, and an object in motion will remain in motion at a constant velocity unless acted upon by an external force.
2. The acceleration of an object depends on the mass of the object and the amount of force applied.
3. For every action, there is an equal and opposite reaction.

Additionally, Newton's law of universal gravitation stated that every point mass attracts every other point mass by a force acting along the line intersecting both points. The force is proportional to the product of the two masses and inversely proportional to the square of the distance between them.

Newton law of universal gravitation is important for understanding the motion of celestial bodies. It predicts that the velocity between objects approaches zero as the distance between them increases, approximately as $v \propto \frac{1}{\sqrt{r}}$. However, empirical observations have shown otherwise. This can be seen in Figure 1.1, which shows the orbital velocity of stellar bodies around the galactic center of Messier 77, also known as NGC 1068 and the Squid galaxy. The initial increase in velocity in the range of 0 – 1 kpc from the galactic center is expected, since the force acting on stellar bodies is proportional to the mass enclosed within their orbits. At larger distances the orbital velocity flattens out, which contradicts Newton's theory, as the orbital velocity should go to zero as the distance from the galactic center keeps increasing. This can mean one of two things: Newton's theory is incorrect or the observations do not tell the entire story.

One way of fixing the discrepancy between Newton's theory and empirical observations is by assuming that there is matter inside and surrounding the galaxy that cannot be directly observed from light emitted by astrophysical objects, which is referred to as dark matter (Persic et al., 1996; Arbey and Mahmoudi, 2021). This dark matter is believed to interact with baryonic matter only by gravitational interactions. There are still many unsolved problems for dark matter, such as I) The "Missing Satellite Problem"

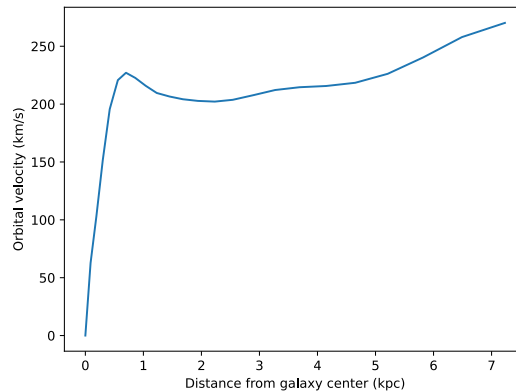


Figure 1.1: The observed orbital velocity of celestial bodies in Messier 77, also known as NGC 1068 and the Squid galaxy.

points to a significant discrepancy between cosmological simulations and observations of dark matter (Perivolaropoulos and Skara, 2022). Simulations based on the Lambda Cold Dark Matter (Λ CDM) model predict thousands of small dark matter satellites around galaxies like the Milky Way. However, far fewer of these satellites are observed astronomically. II) The "core-cusp" problem (de Blok, 2010) is an issue that arises when comparing theoretical predictions of dark matter distributions with empirical observations. Numerical simulations based on cold dark matter predict that the density of dark matter towards the center of galaxies should sharply increase, called cusps. Observations, however, show more uniform distributions of dark matter near the center, which is the core. III) The "Too Big to Fail" problem refers to a significant mismatch between theoretical predictions and astronomical observations regarding the most massive dark matter satellites of galaxies (Perivolaropoulos and Skara, 2022). Theoretical models based on the Λ CDM framework predict that these satellites should have higher densities than what is actually observed.

In addition to these three unsolved problems, there are many more (Perivolaropoulos and Skara, 2022), indicating that it may be reasonable to modify Newton's theory rather than adding matter that is not directly observable. Hence, Milgrom M., in 1983, proposed a theory called MOdified Newtonian Dynamics (MOND), which directly modifies Newton's theory without introducing any new matter (Milgrom, 1983b). MOND modifies the Lagrangian density for Newtonian gravity such that it is no longer quadratic in the potential gradient, which leads to a non-linearity in the acceleration of stellar bodies. There are several Lagrangians to choose from, one of which is the AQUAdratic Lagrangian (AQUAL). This modification is able to explain how the orbital velocity flattens out at distances far from the galactic center, as in Figure 1.1. It accomplishes this by altering the acceleration behavior of stellar bodies in the limit of low Newtonian accelerations while maintaining Newtonian behavior at high accelerations.

Like Newtonian dynamics, MOND can only be solved analytically in a few select cases. Hence, in most cases, numerical methods are required. One such method is the Particle Mesh (PM) method (Hockney and Eastwood, 1988). This method involves discretizing space into a grid of cells where each cell represents a volume of space. Stellar bodies, also referred to as particles due to their small size compared to the cells, within the grid are then assigned to the vertices of nearby cells. This grid allows for the use of discrete Fourier transforms, which simplifies the calculation of the Newtonian potential and gravitational field. Modern techniques such as Tree-code (Barnes and Hut, 1986) or the Fast Multipole Method, which more accurately handle non-uniform particle distributions, have superseded the particle mesh method in traditional Newtonian Dynamics (ND) simulations. However, it remains crucial for MOND because of its ability to manage the introduced nonlinearity by calculating the gravitational potential everywhere simultaneously.

A major downside of the traditional PM method is its inability to accurately determine gravitational potentials and fields whenever two bodies are in close proximity, due to overlap in mass density from Gaussian smoothing. Hence, this paper aims to do three things:

1. Increase the accuracy of the traditional PM method for Newtonian dynamics

2. Implement these improvements in an existing PM implementation for MOND (de Nijs et al., 2023).
3. Apply the improved PM to galaxy models as a proof of concept.

In Chapter 2, both Newtonian dynamics and MOND are introduced. Starting from Newton's law of universal gravitation, Poisson's equation is derived, relating the gravitational potential and mass density. Several relationships between the energies are derived, such as the Virial theorem and the total energy using the Newtonian Lagrangian. Then, MOND is described by modifying the Newtonian Poisson and Lagrangian equations. For both theories, analytical solutions for the gravitational potential and field of a point mass and a Gaussian distribution are derived. Chapter 3 introduces the particle mesh method, including how to correct the acceleration of particles where the traditional particle mesh fails. For this, Fourier transformations are used to calculate the gravitational potential on a grid. Using a central finite difference or spectral method, the gravitational field is determined. Then, using interpolation with a Gaussian weight, the gravitational field can be determined everywhere within the grid. As this method is not accurate whenever two particles are in close proximity because of overlapping mass density, short-range corrections are introduced to correct the acceleration of particles, which are based on analytical solutions. Finally, an iterative process to determine the MOND potential and gravitational fields is described. Chapter 4 discusses the Plummer and Miyamoto-Nagai models, which represent a sphere and disk, respectively, and how to sample them using probabilistic methods. In Chapter 5 all improvements to the numerical methods are tested and compared with analytical expressions determined in earlier chapters. Finally, Chapter 6 will end this paper with some conclusions and further research recommendations.

2

Theory

This chapter explores the theories of Newtonian and modified Newtonian dynamics. Starting with Newtonian dynamics, Poisson's equation is derived from Newton's law of universal gravitation, and then again using the Lagrangian for Newtonian gravity. For MOND, an alternative for Poisson's equation is derived using AQUAL. Both theories are used to derive analytical expressions for a point mass and Gaussian distribution, which will be used in Chapters 3 and 5 to create and test an improved PM method.

2.1. Newtonian Dynamics

In 1687, Isaac Newton described the gravitational interaction between objects in his book *Philosophiæ Naturalis Principia Mathematica* (Newton, 1687). Newton stated that the gravitational force between two objects is proportional to the product of the two masses divided by their squared distance. The first accurate measurement of this proportionality constant was done by the Cavendish experiment, with many improvements over the years, giving us the following equation for Newton's law of universal gravitation for point masses:

$$F_{1,2}(r) = G \frac{M_1 M_2}{r^2}, \quad (2.1)$$

where $F_{1,2}$ is the force acting on two point masses with mass M_1 and M_2 , r is the distance between the two masses in meters, and the gravitational constant $G \approx 6.6743 \cdot 10^{-11} m^3 kg^{-1} s^{-2}$.

$$F_1 = M_1 a \quad (2.2)$$

Newton's law of motion (Newton, 1687) states that the force acting on a point mass is equal to the acceleration multiplied by its mass, as shown in Equation (2.2), with a being the acceleration in ms^{-2} . Now, by Equation (2.1) and (2.2) the acceleration on mass M_1 due to all other matter can be determined. The linearity of the acceleration in Equation (2.2) ensures that the force acting on M_1 is given by the sum of the accelerations caused by all other matter.

As both Equations (2.1) and (2.2) are in a scalar form, it is convenient to transform them into their vector form:

$$\mathbf{F}_{1 \rightarrow 2} = G \frac{M_1 M_2}{|\mathbf{r}|^2} \hat{\mathbf{r}}, \quad (2.3)$$

$$\mathbf{F}_{1 \rightarrow 2} = M_2 \mathbf{a}, \quad (2.4)$$

where the symbols in bold represent vectors in \mathbb{R}^3 , $\mathbf{F}_{1 \rightarrow 2}$ means the force acting on M_2 due to M_1 , $\hat{\mathbf{r}}$ is the unit vector of $\mathbf{r} = \mathbf{r}_1 - \mathbf{r}_2$, and $|\cdot|$ the L_2 norm. Using only these two equations it is possible to determine all possible forces.

However, if there are n point masses and each mass requires taking the sum over $n - 1$ other masses, the computational cost becomes $\mathcal{O}(n^2)$. Therefore, in Chapter 3 methods are introduced to reduce this to $\mathcal{O}(n \log n)$. This requires some additional theory, which makes use of the Newtonian gravitational field \mathbf{g}_N and the Newtonian gravitational potential Φ_N .

The Newtonian gravitational field \mathbf{g}_N is defined as a vector field that represents the gravitational force per unit mass exerted by a given mass distribution at any point in space. It describes how the Newtonian gravitational force is distributed throughout space. For a point mass with mass M , the Newtonian gravitational field created by this mass is given by Equation (2.5),

$$\mathbf{g}_N(\mathbf{r}) = -\frac{GM}{|\mathbf{r}|^2} \hat{\mathbf{r}}, \quad (2.5)$$

where \mathbf{r} is the vector from the location of the mass to any other location in space. This means that, due to the negative sign in Equation (2.5), the gravitational field is pointed towards the mass, and that any other mass at any other location in space receives a force in the direction of the first mass. Note that Equation (2.5) follows from Equations (2.3) and (2.4) and represents an acceleration.

The Newtonian gravitational potential Φ_N represents the work done per unit mass by an external force to bring a small test mass from infinity to any point in space. Theorem 2.1.2 will show that for a point mass, the Newtonian gravitational potential at any distance away from this mass is given by equation (2.6).

$$\Phi_N(r) = -\frac{GM}{r} \quad (2.6)$$

The conservation of total energy in any gravitational system is required. Hence, determining the total energy is also required to be able to check whether it remains constant over time. When dealing exclusively with point masses, the only relevant forms of energy are the kinetic and gravitational potential energies.

The total kinetic energy is linear, meaning that the kinetic energies of all the masses are simply summed to obtain the total kinetic energy. For a single mass, the kinetic energy is given by Equation (2.7), where v is the velocity in ms^{-1} .

$$E_{kin} = \frac{1}{2} M v^2 \quad (2.7)$$

The total gravitational potential energy is also linear and is determined for a single point mass by Equation (2.6), by multiplying it with any other point mass and then taking the sum over these masses, while correcting for double counting.

Now, the total energy is given by the sum of potential and kinetic energies

$$E_{tot} = E_{pot} + E_{kin}. \quad (2.8)$$

In Newtonian dynamics, the Virial theorem can be used to form a fixed relation between the long-term averages of the potential, kinetic, and total energies of point masses.

Theorem 2.1.1 (Virial theorem). *For bound systems in Newtonian dynamics, the long-term average, denoted by $\langle \cdot \rangle$, of the gravitational potential and kinetic energies of point masses is related by*

$$\langle E_{pot} \rangle = -2 \langle E_{kin} \rangle, \quad (2.9)$$

and related to the total energy by

$$\langle E_{tot} \rangle = - \langle E_{kin} \rangle = \frac{1}{2} \langle E_{pot} \rangle \quad (2.10)$$

Proof. The kinetic energy of a Newtonian system is the sum of individual kinetic energies and can be written as follows.

$$E_{kin} = \frac{1}{2} \frac{d^2}{dt^2} \sum_i M_i \mathbf{r}_i^2 = \frac{d}{dt} \sum_i M_i \mathbf{r}_i \cdot \frac{d\mathbf{r}_i}{dt} = \sum_i M_i \left(\mathbf{r}_i \cdot \frac{d^2 \mathbf{r}}{dt^2} + \left(\frac{d\mathbf{r}}{dt} \right)^2 \right)$$

The first term of the rightmost sum can be rewritten as force, so that

$$\sum_i \mathbf{r}_i \cdot \mathbf{F}_i = \frac{1}{2} \frac{d^2}{dt^2} \sum_i M_i \mathbf{r}_i^2 - \sum_i M_i \left(\frac{d\mathbf{r}_i}{dt} \right)^2.$$

Note that the term on the left of the equality is the potential energy. Now, to get the desired result it must be shown that the first term on the right is zero after taking a long time average.

$$\begin{aligned} \left\langle \frac{1}{2} \frac{d^2}{dt^2} \sum_i M_i \mathbf{r}_i^2 \right\rangle &= \lim_{t' \rightarrow \infty} \frac{1}{t'} \int_0^{t'} \frac{1}{2} \frac{d^2}{dt^2} \sum_i M_i \mathbf{r}_i^2 dt \\ &= \lim_{t' \rightarrow \infty} \frac{\frac{d}{dt} \left[\sum_i M_i \mathbf{r}_i^2 \right]_0^{t'}}{2t'} = 0 \end{aligned}$$

The last equality holds because the system is bounded, ensuring that the numerator remains consistently bounded as well. Thus, $\langle E_{pot} \rangle = -2 \langle E_{kin} \rangle$. Now, using Equation (2.8) results in Equations (2.9) and (2.10). □

Up to now, only point masses have been considered. Since any mass is composed of a multitude of tiny particles, it can be mathematically represented as an infinite set of point masses, characterized by its density ρ . To derive Poisson's equation, which connects the density and the gravitational potential, the divergence of the Newtonian gravitational field needs to be determined. A problem arises because the gravitational field goes to infinity as the distance approaches zero. This leads to a non-physical result as an infinite gravitational field means that any two masses moving infinitely close to each other gain an infinite force. Then, according to Equation (2.4), this leads to either an infinite mass or an infinite acceleration. The first is not possible as the mass is pre-defined, and the second is impossible as it would mean infinite velocity, which breaks the fact that objects cannot move faster than the speed of light. Therefore, for taking the divergence of the gravitational field employing Dirac delta-functions is required to allow the divergence of the gravitational field to have a value at zero distances.

Lemma 2.1.1. Consider the vector field $\mathbf{B} : \mathbb{R}^3 \setminus \{0\} \rightarrow \mathbb{R}^3$ defined by

$$\mathbf{B}(\mathbf{r}) = \frac{\mathbf{r}}{|\mathbf{r}|^3}.$$

This is of the same form as equation (2.5) by using the definition $\hat{\mathbf{r}} = \frac{\mathbf{r}}{|\mathbf{r}|}$. The divergence of \mathbf{B} , denoted by $\nabla \cdot \mathbf{B} : \mathbb{R}^3 \rightarrow \mathbb{R}^3$, in the sense of distributions is given by

$$\nabla \cdot \mathbf{B}(\mathbf{r}) = 4\pi\delta(\mathbf{r}),$$

where $\delta(\mathbf{r})$ is the Dirac delta function centered at the origin of \mathbb{R}^3 . This function is defined as a distribution that satisfies

$$\int_{\mathbb{R}^3} \delta(\mathbf{r}) f(\mathbf{r}) d\mathbf{r} = f(0)$$

for all $f \in C_0^\infty(\mathbb{R}^3)$, the space of smooth functions with compact support.

Proof. Consider a sphere S of radius R centered at the origin of \mathbb{R}^3 , and let $\mathbf{B}(\mathbf{r}) = \frac{\mathbf{r}}{|\mathbf{r}|^3}$ be a vector field defined for $\mathbf{r} \neq 0$.

The flux ϕ of the vector field \mathbf{B} through the surface S is calculated by the surface integral:

$$\phi = \oint_S \mathbf{B} \cdot d\mathbf{A}.$$

Substituting the expressions for \mathbf{B} and $d\mathbf{A}$ in spherical coordinates:

$$\phi = \oint_S \frac{r}{r^3} r^2 \sin(\theta) d\theta d\phi = \oint_S \sin(\theta) d\theta d\phi.$$

Simplifying, we find:

$$\phi = \oint_S \sin(\theta) d\theta d\phi = \int_0^{2\pi} \int_0^\pi \sin(\theta) d\theta d\phi = 2\pi [-\cos(\theta)]_0^\pi = 4\pi.$$

According to the divergence theorem for surface to volume integrals:

$$\phi = \iiint_V \nabla \cdot \mathbf{B} dV,$$

where V is the volume enclosed by S . Given that $\phi = 4\pi$ for any sphere of radius R , and acknowledging the singular behavior of \mathbf{B} at the origin when $r = 0$ is allowed, the divergence of \mathbf{B} in the sense of distributions must satisfy:

$$\nabla \cdot \mathbf{B} = 4\pi\delta(\mathbf{r}),$$

where $\delta(\mathbf{r})$ is the Dirac delta function centered at the origin, representing a point source. \square

Now, by using Lemma 2.1.1, taking the divergence of the gravitational field links the gravitational field to the mass density.

Corollary 2.1.1. *The divergence of the Newtonian gravitational field $\mathbf{g}(\mathbf{r})$ at a location \mathbf{r} generated by a mass distribution is proportional to the mass density $\rho(\mathbf{r})$, expressed as:*

$$\nabla \cdot \mathbf{g}_N(\mathbf{r}) = -4\pi G\rho(\mathbf{r}). \quad (2.11)$$

Proof. Starting from the superposition principle, the gravitational field $\mathbf{g}(\mathbf{r})$ at a location \mathbf{r} due to a mass distribution can be determined by integrating the contributions from all points within that mass, leading to the equation:

$$\mathbf{g}(\mathbf{r}) = -G \int_{\mathbb{R}^3} \rho(\mathbf{s}) \frac{\mathbf{r} - \mathbf{s}}{|\mathbf{r} - \mathbf{s}|^3} d^3\mathbf{s}.$$

Leveraging Lemma 2.1.1, and taking the divergence on both sides, we find the relationship between the gravitational field and the mass density

$$\nabla \cdot \mathbf{g}(\mathbf{r}) = -4\pi G \int_{\mathbb{R}^3} \rho(\mathbf{s}) \delta(\mathbf{r} - \mathbf{s}) d^3\mathbf{s} = -4\pi G\rho(\mathbf{r}).$$

\square

The result from Corollary 2.1.1 can be further simplified by linking the gravitational potential and density instead, which results in Poisson's equation.

Corollary 2.1.2. *Poisson's equation for the Newtonian gravitational potential Φ_N is giving by:*

$$\nabla^2 \Phi_N(\mathbf{r}) = 4\pi G\rho(\mathbf{r}) \quad (2.12)$$

Proof. Taking the gradient of the Newtonian gravitational field from Equation (2.5) links the gravitational field to the gravitational potential

$$\nabla\Phi(\mathbf{r}) = \frac{GM}{|\mathbf{r}|^2} \hat{\mathbf{r}} = -\mathbf{g}_N(\mathbf{r}).$$

Now, using Corollary 2.1.1 directly leads to the required result:

$$-\nabla \cdot \mathbf{g}_N(\mathbf{r}) = -\nabla \cdot (-\nabla\Phi(\mathbf{r})) = \nabla^2\Phi(\mathbf{r}) = 4\pi G\rho(\mathbf{r}).$$

\square

2.1.1. Analytical solutions

For any mass density profile, the Newtonian gravitational field, acceleration, and force are known after solving Poisson's equation. Solving Poisson's equation analytically can only be done in a few select cases. Two such analytical solutions will be proven, one for a point mass and one for a Gaussian distribution. Determining the gravitational potential for a point mass is not difficult but will show that the gravitational potential is given by Equation (2.6).

Theorem 2.1.2. *The Newtonian gravitational potential of a point mass M at a distance r from the mass is given by:*

$$\Phi_N(r) = -\frac{GM}{r}. \quad (2.13)$$

Proof. Given a point mass M that is located at the origin, it has a density profile that is given by $\rho(\mathbf{x}) = M\delta^3(\mathbf{x})$. Then, substituting this into Poisson's equation and integrating both sides over a small spherical volume containing the origin results in:

$$\nabla^2\Phi = 4\pi GM\delta^3(\mathbf{x}).$$

$$\int_V \nabla^2\Phi dV = 4\pi GM \int_V \delta^3(\mathbf{x}) dV.$$

Using the divergence theorem on the left-hand side, we get:

$$\oint_{\partial V} \nabla\Phi \cdot d\mathbf{A} = 4\pi GM.$$

For a spherically symmetric potential, this reduces to

$$4\pi r^2 \frac{d\Phi}{dr} = 4\pi GM$$

Integrating with respect to r gives:

$$\Phi(r) = -\frac{GM}{r} + C \quad \text{for } r \neq 0.$$

To determine the integration constant C , we use the boundary condition $\Phi(r) \rightarrow 0$ as $r \rightarrow \infty$. Thus, $C = 0$, resulting in:

$$\Phi(r) = -\frac{GM}{r}.$$

□

A common method in particle mesh simulations is the use of Gaussian smoothing, that is: point masses are replaced by Gaussian distributions (Darden et al., 1993; Yao and Capecelatro, 2021). Due to the spherical symmetry of Gaussian distributions, the Newtonian gravitational potential and field result in a surprisingly simple analytical solution without the need to solve Poisson's equation directly.

Theorem 2.1.3. *Let the mass density of an object be given by a Gaussian distribution*

$\rho(r) = \frac{M}{(2\pi\sigma^2)^{3/2}} e^{-\frac{r^2}{2\sigma^2}}$. *Then, the Newtonian gravitational potential and field are given by*

$$\Phi_N(r) = -\frac{GM}{r} \operatorname{erf}\left(\frac{r}{\sqrt{2}\sigma}\right), \quad (2.14)$$

and

$$\mathbf{g}_N(r) = -\nabla\left(-\frac{GM}{r} \operatorname{erf}\left(\frac{r}{\sqrt{2}\sigma}\right)\right) = GM\left(\frac{\sqrt{2/\pi}}{r\sigma} e^{-\frac{r^2}{2\sigma^2}} - \frac{1}{r^2} \operatorname{erf}\left(\frac{r}{\sqrt{2}\sigma}\right)\right) \hat{\mathbf{r}}, \quad (2.15)$$

respectively, where $\operatorname{erf}(x)$ represents the error function.

Proof. Let $\rho(r) = \frac{M}{(2\pi\sigma^2)^{3/2}} e^{-\frac{r^2}{2\sigma^2}}$ be a Gaussian distribution that represents the density of an object with mass M . Now, instead of solving Poisson's equation, Equation (2.5) is used to calculate the gravitational field directly.

$$\begin{aligned} \mathbf{g}_N(r) &= -G \frac{\mathbf{r}}{|\mathbf{r}|^3} \int_{\mathbb{R}^3} \rho(\mathbf{r}') d^3\mathbf{r}' \\ &= -G \frac{\hat{\mathbf{r}}}{r^2} \int_0^r 4\pi r'^2 M \frac{e^{-r'^2/(2\sigma^2)}}{(2\pi\sigma^2)^{3/2}} dr' \\ &= GM \left(\frac{\sqrt{2/\pi}}{r\sigma} e^{-\frac{r^2}{2\sigma^2}} - \frac{1}{r^2} \operatorname{erf}\left(\frac{r}{\sqrt{2}\sigma}\right) \right) \hat{\mathbf{r}}. \end{aligned}$$

As $\mathbf{g}_N(r) = -\nabla\Phi(r)$ the potential can be found by integrating the gravitational field from 0 to r , resulting in:

$$\Phi_N(r) = -\frac{GM}{r} \operatorname{erf}\left(\frac{r}{\sqrt{2}\sigma}\right).$$

□

2.1.2. Newtonian Lagrangian

Another way of deriving Poisson's equation is by using the Lagrangian density for Newtonian gravity, which is given by:

$$\mathcal{L}(\Phi_N, \nabla\Phi_N) = -\frac{1}{8\pi G} (\nabla\Phi_N)^2 - \rho\Phi_N, \quad (2.16)$$

which is of the form $\mathcal{L} = T_1 + T_2 - V$, where $T_{1,2}$ and V represent kinetic and potential terms, respectively. The minus sign in front of the second term in Equation (2.16) would often indicate that this is a potential term. However, in Equation (2.23) we show that this is indeed a kinetic term.

Using an Euler-Lagrange equation it is possible to derive Poisson's equation:

$$\frac{\partial \mathcal{L}(\Phi_N, \nabla\Phi_N)}{\partial \Phi_N} = \nabla \cdot \left(\frac{\partial \mathcal{L}(\Phi_N, \nabla\Phi_N)}{\partial (\nabla\Phi_N)} \right), \quad (2.17)$$

$$-\rho = -\frac{1}{4\pi G} \nabla \cdot \nabla\Phi_N = -\frac{1}{4\pi G} \nabla^2\Phi_N. \quad (2.18)$$

Now, rearranging the terms shows that $\nabla^2\Phi_N = 4\pi G\rho$.

The Lagrangian does not explicitly depend on time. This implies that the system is invariant under time translations. According to Noether's theorem, this symmetry leads to the conservation of energy. Then, the Hamiltonian that corresponds to this Lagrangian is given by Equation (2.19).

$$\mathcal{H}(\Phi_N, \nabla\Phi_N) = E_{\mathcal{L}}(\Phi_N, \nabla\Phi_N) = -\mathcal{L}(\Phi_N, \nabla\Phi_N) \quad (2.19)$$

Filling in the Hamiltonian results in the following energy relation for the total energy density:

$$\begin{aligned} E_{\text{tot}} &= \frac{1}{2} \sum_i m_i v_i^2 + \frac{1}{8\pi G} \int (\nabla\Phi_N(\mathbf{x}))^2 d^3\mathbf{x} + \int \rho(\mathbf{x})\Phi_N(\mathbf{x}) d^3\mathbf{x} \\ &= E_{\text{kin}} + E_{\text{field}} + E_{\text{pot}}, \end{aligned} \quad (2.20)$$

where E_{kin} , E_{grav} , and E_{pot} are the kinetic, field, and potential energy densities. The first term in the total energy, the kinetic energy, does not originate from the Lagrangian and represents the energy in the velocity of point masses.

It is possible to relate the potential and field energies. The gravitational field energy density is given by:

$$E_{\text{field}} = \int \frac{1}{8\pi G} (\nabla\Phi_N(\mathbf{x}))^2 d^3\mathbf{x}. \quad (2.21)$$

Using partial integration, this integral can be rewritten to contain the Poisson equation,

$$\frac{1}{8\pi G} \int (\nabla\Phi_N(\mathbf{x}))^2 d^3\mathbf{x} = \frac{1}{8\pi G} \left(\int \Phi_N(\mathbf{x}) \nabla\Phi_N(\mathbf{x}) \cdot d\mathbf{A} - \int \Phi_N(\mathbf{x}) \nabla^2\Phi_N(\mathbf{x}) d^3\mathbf{x} \right), \quad (2.22)$$

where the first term on the right is zero, due to zero boundary conditions. Now, filling in the Poisson equation on the right we obtain:

$$E_{\text{field}} = \frac{1}{8\pi G} \int (\nabla\Phi_N(\mathbf{x}))^2 d^3\mathbf{x} = -\frac{1}{2} \int \rho(\mathbf{x}) \Phi_N(\mathbf{x}) d^3\mathbf{x} = -\frac{1}{2} E_{\text{pot}}. \quad (2.23)$$

As the potential energy is always defined to be negative, the field energy is always positive. This shows that the second term in Equation (2.16) is a kinetic term.

Since the Lagrangian primarily involves fields rather than direct interactions between point masses, deriving the Virial theorem directly from it is not straightforward, and only works for point masses.

2.2. Modified Newtonian Dynamics

Theorem 2.1.2 shows that the Newtonian potential goes to zero when the distance from a mass goes to infinity, meaning that the gravitational influence of a mass decays as $\frac{1}{r}$ towards infinite distances.

This shows that, without the use of dark matter, the orbital velocities in galaxies must go to zero as $\frac{1}{\sqrt{r}}$ beyond their boundaries, which they do not, as can be seen in Figure 1.1.

MOND was proposed by Milgrom in 1983 (Milgrom, 1983b) as a theory to address this discrepancy. MOND modifies Poisson's equation by introducing an additional term to the Newtonian Lagrangian in Equation (2.16). This leads to a modified version of Poisson's equation, which is from now on referred to as the MOND Poisson equation, and is derived in Section 2.2.2, is given by:

$$\nabla \cdot \left(\mu \left(\frac{|\nabla\Phi_M|}{a_0} \right) \nabla\Phi_M \right) = 4\pi G\rho, \quad (2.24)$$

where μ , known as the interpolation function, incorporates the constant $a_0 \approx 1.2 \cdot 10^{-10} m_s^{-2}$. The role of the interpolation function μ is to modify the gravitational potential so that it is in agreement with the empirically measured rotation curves.

Close to the center of galaxies the empirical measurements based solely on visible matter and Newtonian dynamics match. At these distances the acceleration is large, meaning that the MOND Poisson equation should return the Newtonian Poisson equation in the limit of high accelerations. That is $\mu \left(\frac{|\nabla\Phi_M|}{a_0} \right) \approx 1$, when $|\nabla\Phi_M| \gg a_0$ and is referred to as the Newtonian regime. In the limit of low accelerations, thus at a great distance from a galaxy center, Milgrom proposes that the interpolation function should become linear with the accelerations: $\mu \left(\frac{|\nabla\Phi_M|}{a_0} \right) \approx \frac{|\nabla\Phi_M|}{a_0}$ when $|\nabla\Phi_M| \ll a_0$, called the deep-MOND regime. When looking only at a single point mass, this threshold occurs at a distance $r_T = \sqrt{\frac{GM}{a_0}}$. Thus, to be entirely in the Newtonian or deep-MOND regime, the distances should be much smaller than or greater than r_T , respectively.

2.2.1. Choosing an interpolation function

Now, to use MOND, an interpolation function must be chosen. One interpolation function proposed by Milgrom, called the standard interpolation function, is given by (Milgrom, 1983a):

$$\mu(x) = \frac{x}{\sqrt{1+x^2}}. \quad (2.25)$$

However, Milgrom's selection for this function was arbitrary. Therefore, a closer examination of alternative families of interpolation functions is necessary. Using this proposed interpolation function it is possible to create a family of similar functions (Milgrom and Sanders, 2008):

$$\mu_n(x) = \frac{x}{(1+x^n)^{1/n}}, \quad (2.26)$$

with μ_2 giving back the original interpolation function proposed by Milgrom.

For a slow transition between the Newtonian regime and deep-MOND regimes, one can choose the function μ_1 , also called the "simple" interpolation function (Gentile et al., 2011) as it has a simple analytical form. However, this function is only compatible with very few galactic rotation curves, such as NGC 3198, and fails in the limit of large distances from the galactic center (Famaey and Binney, 2005; Zhao and Famaey, 2006).

An approximation for the MOND gravitational field, is by relating it to the Newtonian gravitational field via the inverse of the interpolation function ν (Milgrom and Sanders, 2008), such that

$$\mathbf{g}_M = \nu \left(\frac{|\mathbf{g}_N|}{a_0} \right) \mathbf{g}_N, \quad (2.27)$$

where is used that $|\nabla\Phi_M| = |\mathbf{g}_N|$. For systems of one-dimensional or spherical symmetry, this approximation is, in fact, exact (Milgrom, 2010).

For the Milgrom family of interpolation functions (2.26), the inverse of the interpolation functions, referred to as inverse interpolation functions, are given by:

$$\nu_n(y) = \left(\frac{1 + (1 + 4y^{-n})^{1/2}}{2} \right)^{1/n}, \quad (2.28)$$

where $y = \frac{|\mathbf{g}_N|}{a_0}$.

Another family of interpolation functions, introduced by McGaugh (McGaugh, 2008), starts by defining the inverse interpolation function instead,

$$\nu_m(y) = (1 - \exp(-y^{m/2}))^{-1/m}, \quad (2.29)$$

where ν_m is the inverse function of μ_m . However, a drawback of this family is that finding the interpolation function μ_m requires inverting ν_m which might not be possible analytically, necessitating the use of numerical methods.

As both the simple interpolation function is not suitable, and the McGaugh interpolation function is not analytically known, $\mu_2 = \frac{x}{\sqrt{1+x^2}}$ is chosen for this paper. The benefit of this function is that it is possible, as in the Newtonian case, to calculate the potential and field analytically for a point mass and for a Gaussian distribution.

2.2.2. MOND Lagrangian

Now, to derive the MOND Poisson equation, the corresponding AQuadratic Lagrangian (AQUAL) is given by:

$$\mathcal{L}(\Phi_M, \nabla\Phi_M) = -\frac{a_0^2}{8\pi G} f \left(\frac{|\nabla\Phi_M|^2}{a_0^2} \right) - \rho\Phi_M,$$

Similar to derivation of the Newtonian Poisson equation from the Newtonian Lagrangian, an Euler-Lagrange equation is used:

$$\frac{\partial \mathcal{L}(\Phi_M, \nabla\Phi)}{\partial \Phi_M} = \nabla \cdot \left(\frac{\partial \mathcal{L}(\Phi_M, \nabla\Phi_M)}{\partial (\nabla\Phi_M)} \right),$$

resulting in:

$$\begin{aligned} -\rho &= \frac{a_0^2}{8\pi G} \nabla \cdot \left(\frac{2(\nabla\Phi_M)^2}{a_0^2} f' \left(\frac{(\nabla\Phi_M)^2}{a_0^2} \right) \right) \\ &= -\frac{1}{4\pi G} \nabla \cdot \left(\mu \left(\frac{|\nabla\Phi_M|}{a_0} \right) \nabla\Phi_M \right), \end{aligned}$$

where $f' \left(\frac{|\nabla\Phi_M|^2}{a_0^2} \right) = \mu \left(\frac{|\nabla\Phi_M|}{a_0} \right)$ is the interpolation function. Rearranging the terms leads to the MOND Poisson equation.

It is important to determine the total energy of the system to check whether it remains constant over time. This is done under the assumption of the standard interpolation function, as the next section will provide analytical solutions to the MOND Poisson equation under this assumption. To start, the function f must be found. For the standard interpolation function, we have the following.

$$\mu \left(\frac{|\nabla\Phi_M|}{a_0} \right) = \frac{\frac{|\nabla\Phi_M|}{a_0}}{\sqrt{1 + \left(\frac{|\nabla\Phi_M|}{a_0} \right)^2}}.$$

To find the corresponding $f(u)$, where $u = \frac{|\nabla\Phi_M|^2}{a_0^2}$, we express it as:

$$f \left(\frac{|\nabla\Phi_M|^2}{a_0^2} \right) = \int \sqrt{\frac{u}{1+u}} du = \sqrt{u^2 + u} - \operatorname{arcsinh}(\sqrt{u}), \quad (2.30)$$

where the integration constant is set to zero. The Hamiltonian density \mathcal{H} is given by:

$$\mathcal{H}(\Phi_M, \nabla\Phi_M) = -\mathcal{L}(\Phi_M, \nabla\Phi_M).$$

So, the total energy density, after including the kinetic energy due to the velocity of the masses, becomes:

$$E_{tot} = \frac{1}{2} \sum_i m_i v_i + \int \frac{a_0^2}{8\pi G} f \left(\frac{|\nabla\Phi_M(\mathbf{x})|^2}{a_0^2} \right) d^3\mathbf{x} + \int \rho(\mathbf{x}) \Phi_M(\mathbf{x}) d^3\mathbf{x}, \quad (2.31)$$

where f is now given by Equation (2.30). Note that, compared to Equation (2.20), only the calculation of the field energy has changed.

2.2.3. Analytical solutions

Using the standard interpolation function $\mu_2(x) = \frac{x}{\sqrt{1+x^2}}$ it is possible to find the analytical solution to the MOND Poisson equation in a few select cases. For a general spherical symmetric density profile, the MOND gravitational field can be reduced to a quadratic equation.

Theorem 2.2.1. *Let $\rho(r)$ be a spherically symmetric density profile. Then, the MOND Poisson equation reduces to the following quadratic equation*

$$g_M^4(r) - \frac{M(r)G}{r^2} g_M^2(r) - \frac{GM(r)a_0^2}{r^2} = 0, \quad (2.32)$$

where $M(r)$ is the enclosed mass within radius r from the center of the mass density and is given by

$$M(r) = \int_0^r 4\pi\rho(r')r'^2 dr'. \quad (2.33)$$

Proof. Let $\rho(r)$ be a spherically symmetric density profile. Filling in the standard interpolation function in the MOND Poisson equation, and using the fact that $\nabla\Phi(r) = -g_M(r)\hat{\mathbf{r}}$, the MOND Poisson equation reduces to:

$$\nabla \cdot \left(\frac{g_M^2(r)\hat{\mathbf{r}}}{a_0\sqrt{1 + (g_M/a_0)^2}} \right) = 4\pi G\rho(r).$$

To solve this, integrate both sides over a spherical volume of radius r centered at the origin:

$$\int_V \nabla \cdot \left(\frac{g_M^2\hat{\mathbf{r}}}{a_0\sqrt{1 + (g_M/a_0)^2}} \right) dV = \int_V 4\pi G\rho(r) dV.$$

Using the divergence theorem on the left-hand side, we get:

$$\oint_{\partial V} \frac{g_M^2}{a_0 \sqrt{1 + (g_M/a_0)^2}} \hat{\mathbf{r}} \cdot d\mathbf{A} = \int_V 4\pi G \rho(r) dV.$$

For a spherically symmetric potential, this reduces to:

$$4\pi r^2 \frac{g_M^2}{a_0 \sqrt{1 + (g_M/a_0)^2}} \Big|_r = 4\pi GM(r),$$

where $M(r) = \int_0^r 4\pi \rho(r') r'^2 dr'$. Simplifying, we obtain:

$$\frac{g_M^2(r)}{a_0 \sqrt{1 + (g_M/a_0)^2}} = \frac{GM(r)}{r^2}.$$

Squaring both sides and rearranging the terms results in:

$$\left(\frac{g_M^2(r)}{a_0 \sqrt{1 + (g_M/a_0)^2}} \right)^2 = \left(\frac{GM(r)}{r^2} \right)^2.$$

Letting $x = g_M^2$ and solving for x shows that Equation (2.32) is indeed quadratic:

$$x^2 - \frac{GM(r)}{r^2} x - \frac{GM(r)a_0^2}{r^2} = 0.$$

□

Theorem 2.2.1 shows that, under the standard interpolation function and spherical symmetry, the MOND gravitational field can be found by solving a basic quadratic equation. Now, this method is used to analytically determine the MOND gravitational field for a point mass and Gaussian distribution.

Corollary 2.2.1. *The MOND gravitational field, using the standard interpolation function, of a point mass with a density profile $\rho(\mathbf{r}) = M\delta^3(\mathbf{r})$ becomes:*

$$g_M(r) = \sqrt{\frac{GM}{2r^2} + \frac{1}{2} \sqrt{\left(\frac{GM}{r^2}\right)^2 + \frac{4a_0^2 GM}{r^2}}} \quad (2.34)$$

Corollary 2.2.2. *The MOND gravitational field, using the standard interpolation function, of a Gaussian density profile $\rho(r) = \frac{M}{(2\pi\sigma^2)^{3/2}} e^{-r^2/2\sigma^2}$ becomes*

$$g_M(r) = \sqrt{\frac{A^2(r) + \sqrt{A^4(r) + 4a_0^2 A^2(r)}}{2}}, \quad (2.35)$$

where $A(r) = GM \left(\frac{r\sqrt{2/\pi}}{\sigma} e^{-r^2/2\sigma^2} - \operatorname{erf}\left(\frac{r}{\sqrt{2}\sigma}\right) \right)$

A simplification can be made for masses in deep-MOND where $\mu(x) \approx x$. Thus, the gravitational field for a point mass and for a Gaussian distribution are also determined under this condition. The results from using the standard interpolation function should reduce to these in the limit of low accelerations.

Theorem 2.2.2. *In deep-MOND, where $\mu(x) \approx x$, for spherically symmetric density profiles $\rho(r)$, the MOND gravitational field becomes:*

$$g_M(r) = \sqrt{\frac{Ga_0}{r^2} \int_0^r 4\pi \rho(r') r'^2 dr'} = \frac{\sqrt{GM(r)a_0}}{r} \quad (2.36)$$

Proof. In deep-MOND, under the assumption of spherically symmetric density profiles $\rho(r)$, the MOND Poisson equation reduces to

$$\nabla \cdot \left(\frac{g_M^2(r)}{a_0} \right) = 4\pi G\rho(r),$$

which means that the MOND gravitational field can be found with a single integral.

$$\frac{g_M^2(r)}{a_0} = \frac{G}{r^2} \int_0^r 4\pi\rho(r')r'^2 dr' = \frac{GM(r)}{r^2}$$

Then, taking the square root on both sides gives Equation (2.36). \square

The analytical expression of the potential and gravitational field in deep-MOND for both a point particle and Gaussian distribution can be easily determined by using the density integrals from their Newtonian counterparts.

Corollary 2.2.3. *The deep-MOND gravitational field for a point mass with density profile $\rho(r) = M\delta(r)$ is given by*

$$g_M(r) = \frac{\sqrt{GMa_0}}{r} \quad (2.37)$$

Corollary 2.2.3 shows an interesting result. At great distances, any mass can be approximated as a point mass. Then, gravitational potential becomes $\Phi_M(r) = \int_0^r \frac{\sqrt{GMa_0}}{r'} dr' = \sqrt{GMa_0} \log(r)$. This is totally different from the Newtonian case in equation (2.6), where the gravitational potential goes to zero when the distance goes to infinity. For MOND, this does not happen and instead goes to infinity for increasingly large distances. This means that no mass can escape the gravitational influence of any other mass.

An important result is that for masses in a circular orbit around a central mass, the gravitational field acting on the masses due to the central mass is given by the centripetal acceleration $g = \frac{v^2}{r}$. As this is also the MOND gravitational field, Corollary 2.2.3 results in the relation $v^4 = GMa_0$, meaning that the orbital velocity of bodies around a central mass becomes constant at large distances. This is exactly what the empirical measurements show; see Figure 1.1.

Corollary 2.2.4. *The deep-MOND gravitational field for a Gaussian mass density profile, given by $\rho(r) = \frac{M}{(2\pi\sigma^2)^{3/2}} e^{-\frac{r^2}{2\sigma^2}}$ is:*

$$g_M(r) = \sqrt{a_0 \frac{GM}{r^2} \left(\frac{r\sqrt{2/\pi}}{\sigma} e^{-r^2/2\sigma^2} - \operatorname{erf}\left(\frac{r}{\sqrt{2}\sigma}\right) \right)} \quad (2.38)$$

2.2.4. MOND variations

The AQUAL version described above is only one of many possible versions of MOND. one popular form being QUasi-linear MOND (QUMOND) (Milgrom, 2010; Milgrom, 2023). QUMOND changes the above AQUAL formulation into one that simplifies the nonlinearity of AQUAL This is done by using the Newtonian potential as follows:

$$\nabla^2 \Phi_M = \nabla \cdot \left(v \left(\frac{|\nabla \Phi_N|}{a_0} \right) \nabla \Phi_N \right) \quad (2.39)$$

As QUMOND does not entirely remove the non-linearity and requires the the calculations of the Newtonian potential first, it is not an elegant form of MOND and will therefore not be used in this paper.

3

Particle Mesh

In this chapter, numerical methods for solving the Newtonian and MOND Poisson equations are described in detail. Starting with an existing code implementation (de Nijs et al., 2023), strategies for improving the computation of Newtonian and MOND potential and gravitational fields are presented. The Newtonian potential and gravitational field are calculated using the particle mesh method. Then, using the known analytical solution of Theorem 2.1.3, short-range corrections are applied to improve accuracy where needed. Subsequently, the MOND potential and gravitational field are determined through an iterative approach based on the Newtonian gravitational field. The source code that includes all improvements can be found at <https://github.com/MartinVingerhoets/PMCorrections>.

3.1. Particle-Mesh for Newtonian Dynamics

In most cases, the Poisson equation cannot be solved analytically, requiring numerical methods. One such method is the particle mesh method, which combines mass density with a grid-based strategy. Using a grid is beneficial because it enables the use of discrete Fourier transforms. Now, by starting from continuous Fourier transforms, we will see that using Fourier methods is a relatively simple method to calculate the Newtonian gravitational field and potential.

Definition 3.1.1. *The continuous Fourier transform of a function $f : \mathbb{R} \rightarrow \mathbb{C}$, denoted by \tilde{f} or $\mathcal{F}\{f\}$, is given by*

$$\mathcal{F}\{f\}(k) = \tilde{f}(k) = \int_{-\infty}^{\infty} f(x)e^{-ikx} dx,$$

and the inverse Fourier transform is

$$\mathcal{F}^{-1}\{f\}(x) = \frac{1}{2\pi} \int_{-\infty}^{\infty} \tilde{f}e^{ikx} dk.$$

After applying the Fourier transform to a function, it goes from real space to something called k -space, as the space coordinate is integrated away and a new variable k is introduced. Note that the Fourier transform also works for three-dimensional functions by applying the Fourier transform for each dimension. This means that instead of a scalar k , the function f in k space depends instead on a vector \mathbf{k} . A result that will be useful for analytical solutions is Parseval's theorem, which relates the real space of two functions f and g to their k -space counterpart via their inner products.

Theorem 3.1.1 (Parseval's Theorem). *Let $f, g : \mathbb{C} \rightarrow \mathbb{C}$ be functions that are both integrable and square integrable. Then, the inner products of f and g in real and k -space are equal:*

$$\langle f, g \rangle = \langle \tilde{f}, \tilde{g} \rangle,$$

where

$$\langle f, g \rangle = \int_{-\infty}^{\infty} f(x)\overline{g(x)} dx,$$

and

$$\langle \tilde{f}, \tilde{g} \rangle = \int_{-\infty}^{\infty} \tilde{f}(k) \overline{\tilde{g}(k)} dk.$$

Proof. We start by applying the definition of the Fourier transform to the inner product $\langle f, g \rangle$:

$$\langle f, g \rangle = \int_{-\infty}^{\infty} f(x) \overline{g(x)} dx.$$

The Fourier transform of the product $f(x) \overline{g(x)}$ is given by the convolution of $\tilde{f}(k)$ with the complex conjugate of the Fourier transform of $g(x)$, reversed:

$$\mathcal{F}\{f(x) \overline{g(x)}\}(k) = \int_{-\infty}^{\infty} \tilde{f}(u) \overline{\tilde{g}(k-u)} du.$$

By the convolution theorem and changing the order of integration, we can write:

$$\int_{-\infty}^{\infty} \tilde{f}(k) \overline{\tilde{g}(k)} dk = \int_{-\infty}^{\infty} f(x) \overline{g(x)} dx,$$

which confirms the equality of the inner products in both domains. \square

In particle mesh methods, both space and time are discretized (Darden et al., 1993; Yao and Capece-latro, 2021). Therefore, it is not possible to use the continuous Fourier transforms described above. However, it is possible to use the discrete form of the Fourier transform, which transforms a sequence of numbers $\{x_n\} \in \mathbb{C}^n$ into another sequence of numbers $X_k \in \mathbb{C}^n$.

Definition 3.1.2. *In one dimension, the discrete Fourier transform is given by:*

$$X_k = \sum_{n=0}^{N-1} x_n e^{-\frac{i2\pi kn}{N}}, \quad (3.1)$$

where N represents the amount of numbers in the sequence $\{x_n\}$. The inverse transform is then given by:

$$x_n = \frac{1}{N} \sum_{k=0}^{N-1} X_k e^{\frac{i2\pi kn}{N}}.$$

When using a sufficiently large N it is reasonable to assume that the discrete Fourier transform approximates the continuous Fourier transform. However, there are some important differences that must be taken into account. The continuous Fourier transform is defined for the entire domain, whilst the discrete version is not. This leads to the discrete version being periodic and hence contains an infinite number of virtual copies in real space, which is called aliasing. The influence of these copies on each other needs to be prevented, which can be done by taking N such that the data used is surrounded by zeros. For discrete Fourier transforms, it is possible to optimize the numerical computations using Fast Fourier Transforms (FFT) (Cooley and Tukey, 1965), which reduces the computational complexity from $\mathcal{O}(n^2)$ to $\mathcal{O}(n \log(n))$.

To solve the Newtonian Poisson equation numerically, the density needs to be discretised, meaning that a grid needs to be defined. For this, it is necessary to choose a volume in which to place the grid, called the simulation volume. Only objects in the simulation volume are considered in the simulation. In each spatial dimension, this volume is divided into N_x , N_y , and N_z parts. Since the discrete Fourier transform in Equation (3.1) assumes uniform spacing, the length L_x , L_y , and L_z of each edge in the grid must be the same in any given direction. One might consider using nonuniform Fourier transforms (Barnett et al., 2019), but they introduce significant complexity, which is why we will not pursue that approach.

In case of simple simulations with few particles, a cubic grid with $N = N_x = N_y = N_z$ and $L = L_x = L_y = L_z$ is chosen, with each cube referred to as a pixel. However, for a flat spiral galaxy, it is often possible

to reduce the number of pixels in one direction, significantly reducing the total number of pixels and the computational cost of the FFT. The grid is composed of vertices, edges, and cells, which will be denoted as v , e , and c , respectively. Typical values for N range from 64 to 256. It is optimal for N to be a power of 2, but it is possible for N to include a factor 3 or 5, which use slightly different and slower algorithms for the FFT (Yfantis and Borgman, 1981). Increasing the number of pixels beyond 512 in all directions significantly slows the computation of the FFTs and could lead to an out-of-memory problem on some systems.

Each simulation has a set of objects that need to be placed on the grid. For galaxy simulations, L is much larger compared to the size of the placed objects, which means that they can be approximated as point particles.

3.1.1. Calculating the Newtonian potential and gravitational field

Using the continuous Fourier transform, one can solve for the potential in the Newtonian Poisson equation.

Theorem 3.1.2. *The Fourier transform of the Newtonian potential $\Phi_N(\mathbf{r})$ related to the mass density $\rho(\mathbf{r})$ is given by*

$$\tilde{\Phi}_N(\mathbf{k}) = -4\pi G \frac{\tilde{\rho}(\mathbf{k})}{|\mathbf{k}|^2}. \quad (3.2)$$

The Newtonian potential in real space is then recovered by using the inverse Fourier transform:

$$\Phi_N(\mathbf{r}) = \mathcal{F}^{-1} \left\{ -4\pi G \frac{\tilde{\rho}(\mathbf{k})}{|\mathbf{k}|^2} \right\} (\mathbf{r}). \quad (3.3)$$

Proof. We start by recalling the Poisson's equation for the Newtonian potential Φ_N due to a mass distribution ρ :

$$\nabla^2 \Phi_N(\mathbf{r}) = 4\pi G \rho(\mathbf{r}).$$

Taking the Fourier transform of both sides, we have

$$\begin{aligned} \mathcal{F}\{\nabla^2 \Phi_N(\mathbf{r})\} &= \mathcal{F}\{4\pi G \rho(\mathbf{r})\}, \\ -|\mathbf{k}|^2 \tilde{\Phi}_N(\mathbf{k}) &= 4\pi G \tilde{\rho}(\mathbf{k}). \end{aligned}$$

Here, we used the Fourier transform of the Laplace operator ∇^2 , which is $-|\mathbf{k}|^2$. Solving for $\tilde{\Phi}_N(\mathbf{k})$, we find

$$\tilde{\Phi}_N(\mathbf{k}) = -\frac{4\pi G \tilde{\rho}(\mathbf{k})}{|\mathbf{k}|^2}.$$

Finally, the Newtonian potential in real space is obtained by taking the inverse Fourier transform:

$$\Phi_N(\mathbf{r}) = \mathcal{F}^{-1} \left\{ -4\pi G \frac{\tilde{\rho}(\mathbf{k})}{|\mathbf{k}|^2} \right\} (\mathbf{r}).$$

□

By approximating the discrete Fourier transform as the continuous Fourier transform, Theorem 3.1.2 and the analytical expressions derived previously can be used to test the precision of any numerical solution for which an analytical expression is known.

Note that the division of $|\mathbf{k}| = \mathbf{0}$ is not allowed in Theorem 3.1.2 as that would lead to an infinite potential. In Fourier analysis, $\mathbf{k} = \mathbf{0}$ represents the average of the values in real space. To avoid dividing by zero, $\mathbf{k} = 0$ is replaced by $\mathbf{k} = \mathbf{1}$ as a workaround. Then, after division by \mathbf{k} , the value in k -space that would have been divided by zero is set to zero, effectively setting the average of the potential to zero. This means that it is not possible to accurately determine the average of the gravitational potential in real space. An incorrect average does not affect the dynamics of the simulation, as it is only a shift in the potential. This shift is removed when calculating the gravitational field, which is the gradient of the potential. However, it makes the calculation of the potential energy in Equation (2.20) unreliable. Thus, when calculating the potential energy, the relation between the gravitational

potential and field energies from Equation (2.23) must be checked to know if the potential energy is accurate.

Since particles can be placed anywhere within the simulation volume, they do not have to be located at the grid vertices. However, the discrete Fourier transform of the density confines the density function's values to the vertices. Consequently, the mass of each particle must be transferred to the vertices. To do this, the masses of the particles are commonly smoothed onto the grid using a Gaussian distribution (Darden et al., 1993, Yao and Capecelatro, 2021). Using a Gaussian distribution offers several advantages: 1) It matches the 12-th order Cloud-in-Cell method (Hockney and Eastwood, 1988), is spherically symmetric, and separates easily in Cartesian coordinates. Additionally, this smoothing leads to simple analytical expressions for the potential and gravitational field, which is shown in Theorem 2.1.3.

Gaussian smoothing works as follows: A point particle with mass M located at location \mathbf{r} is described with density:

$$\rho(\mathbf{r}_i) = M \frac{e^{-|\mathbf{r}-\mathbf{r}_i|^2/2\sigma^2}}{(2\pi\sigma^2)^{3/2}}, \quad (3.4)$$

with mass assigned to the vertex at location \mathbf{r}_i . Since the density is linear, the masses of all smoothed point particles can be summed. Therefore, when the smoothing regions of two different particles overlap at a vertex, the densities at that vertex are also summed.

For computational simplicity $\sigma = 1$ is chosen. As a Gaussian distribution quickly goes to zero as the distance increases it is possible to limit the vertices for which a mass is applied, shortening the sum for each mass in equation (3.4). For this, a pre-computed set of vertices, representing a ball can be used which is centered at the top left back vertex of the cell in which the particle is located..

Now, using Theorem 3.1.2, calculating the discrete Fourier transform of the density grid allows for an approximated calculation of the Newtonian potential. The gravitational field is represented by the gradient of the potential: $\nabla\Phi_N = -\mathbf{g}_N$. Since the potential is only known on the vertices of the grid, a numerical method must be chosen to determine the gravitational field at the vertices. For this, two different numerical methods are worked out: the central finite difference, and spectral method.

Central finite difference method

The central finite difference method of fourth-order in one dimension is given by:

$$\frac{dg(x)}{dx} \approx \frac{-g(x+2h) + 8g(x+h) - 8g(x-h) + g(x-2h)}{12h} \quad (3.5)$$

where x is the location of the vertex of interest, and $h = \frac{L_x}{N_x}$ represents the distance between vertices. This method has several advantages. This method offers multiple benefits. It achieves higher accuracy as a fourth-order method with an error term of $\mathcal{O}(h^4)$, providing a more precise approximation of the derivative than lower-order methods like the second-order central difference. Its symmetry, characteristic of central difference methods, uses points symmetrically distributed around x , improving numerical stability and accuracy.

Spectral method

Another approach to calculating derivatives is to work in the k -space. This method offers the advantage of keeping the Newtonian potential in k -space, thereby avoiding the need to transform back to the real domain before computing the gravitational acceleration field. By using this technique, the gravitational field in one dimension can be expressed as:

$$\frac{dg(x)}{dx} = \mathcal{F}^{-1}\{ik\tilde{\Phi}_N(k)\} \quad (3.6)$$

It is still required to do an inverse Fourier transform, but multiplication in k -space might be computationally more efficient than using a central finite difference method.

3.1.2. Interpolating back to original particle locations

Since particles do not need to be located at the vertices of the grid, it is necessary to interpolate from the grid back to the original positions of the particles. To maintain consistency, the same Gaussian smoothing from equation (3.4) is used as a weight function for the interpolation, making it possible to reconstruct the gravitational field between the vertices. Due to this weighting, effectively two smoothings have occurred. The first was done by placing a mass onto the grid and the second by interpolating the gravitational field back to a particle. So, the Newtonian gravitational field acting on a particle at location $(0, 0, R)$ due to another smoothed particle located at the origin is given by:

$$g_N((0, 0, R)) = \int_{-\infty}^{\infty} \int_{-\infty}^{\infty} \int_{-\infty}^{\infty} -\nabla\Phi_N(x, y, z) \frac{e^{-(x^2+y^2+(z-R)^2)/2\sigma^2}}{(2\pi\sigma^2)^{3/2}} dx dy dz$$

Solving this integral in Cartesian, spherical, and cylindrical coordinates failed. However, it is possible to solve this using Parseval's theorem.

Theorem 3.1.3. *Let p_1, p_2 be particles at locations $(0, 0, 0)$ and $(0, 0, R)$, respectively. Then, the gravitational potential at the location of particle p_2 due to the smoothed mass of p_1 is given by:*

$$\Phi_N((0, 0, R)) = -GM \frac{\text{erf}\left(\frac{R}{2\sigma}\right)}{R},$$

and the Newtonian gravitational field by:

$$\mathbf{g}_N((0, 0, R)) = GM \left(\frac{e^{-R^2/4\sigma^2}}{\sqrt{\pi}R\sigma} - \frac{\text{erf}\left(\frac{R}{2\sigma}\right)}{R^2} \right) \hat{\mathbf{z}}. \quad (3.7)$$

Proof. Let $f(x, y, z) = -\nabla\Phi(x, y, z)$. Then the Fourier transform of f is given by:

$$\begin{aligned} \tilde{f}(k_x, k_y, k_z) &= \mathcal{F}\{-\nabla\Phi_N(x, y, z)\} \\ &= -i\mathbf{k}\mathcal{F}\{\Phi_N(x, y, z)\} \\ &= -i\mathbf{k} \left(-4\pi G \frac{\tilde{\rho}}{|\mathbf{k}|^2} \right) \\ &= 4\pi M i \frac{\mathbf{k}}{|\mathbf{k}|^2} e^{-\sigma^2(k_x^2+k_y^2+k_z^2)/2} \end{aligned}$$

At location $(0, 0, R)$ we use a Gaussian to interpolate the gravitational field at that location, thus the following shifted Gaussian is used:

$$g(x, y, z) = \frac{e^{-(x^2+y^2+(z-R)^2)/2\sigma^2}}{(2\pi\sigma)^{3/2}}.$$

In k -space this gives also is a Gaussian:

$$\tilde{g}(k_x, k_y, k_z) = \frac{e^{-\sigma^2(k_x^2+k_y^2+k_z^2)/2} e^{ik_z R}}{(2\pi\sigma)^{3/2}}.$$

Now, using Parseval's theorem and solving the integral in k -space results in:

$$\begin{aligned}
\mathbf{g}_N((0, 0, R)) &= \iiint -\nabla\phi(x, y, z) \frac{e^{-(x^2+y^2+(z-R)^2)/2\sigma^2}}{(2\pi\sigma)^{3/2}} dx dy dz \\
&= \iiint -i \frac{4\pi GM}{(2\pi\sigma)^3} \frac{\mathbf{k}}{|\mathbf{k}|^2} e^{-\sigma^2(k_x^2+k_y^2+k_z^2)/2} e^{-\sigma^2(k_x^2+k_y^2+k_z^2)/2} e^{ik_z R} dk_x dk_y dk_z \\
&= \frac{-i4\pi GM}{(2\pi\sigma)^3} \int_0^{2\pi} d\phi \int_{-1}^1 d\cos(\theta) \int_0^\infty k \cos(\theta) e^{iRk \cos(\theta) - \sigma^2 k^2} dk \hat{\mathbf{z}} \\
&= \frac{-i8\pi^2 GM}{(2\pi\sigma)^3} \int_0^\infty k e^{-\sigma^2 k^2} \int_{-1}^1 c e^{iRkc} dc dk \hat{\mathbf{z}} \\
&= \frac{-i8\pi^2 GM}{(2\pi\sigma)^3} \int_0^\infty k e^{-\sigma^2 k^2} \left(\frac{e^{iRk} - e^{-iRk}}{R^2 k^2} - i \frac{e^{iRk} + e^{-iRk}}{Rk} \right) dk \hat{\mathbf{z}} \\
&= \frac{-i8\pi^2 GM}{R^2 (2\pi\sigma)^3} \int_0^\infty e^{-\sigma^2 k^2} \left(\frac{e^{iRk} - e^{-iRk}}{k} - iR (e^{iRk} + e^{-iRk}) \right) dk \hat{\mathbf{z}} \\
&= GM \left(\frac{e^{-R^2/4\sigma^2}}{\sqrt{\pi} R \sigma} - \frac{\operatorname{erf}\left(\frac{R}{2\sigma}\right)}{R^2} \right) \hat{\mathbf{z}},
\end{aligned}$$

giving the desired gravitational field.

Now, the potential can be found by letting R be a variable and integrating from 0 to R , resulting in:

$$\Phi_N((0, 0, R)) = -GM \left(\frac{\operatorname{erf}\left(\frac{R}{2\sigma}\right)}{R} \right).$$

□

Thus, now that the gravitational field at location $(0, 0, R)$ is known, it is possible to determine the gravitational field at any location. Let \mathbf{F} be a vector in \mathbb{R}^3 , then the gravitational field at the location \mathbf{F} is given by:

$$\frac{\mathbf{F}}{|\mathbf{F}|} GM \left(\frac{e^{|\mathbf{F}|^2/4\sigma^2}}{\sqrt{\pi} |\mathbf{F}| \sigma} - \frac{\operatorname{erf}\left(\frac{|\mathbf{F}|}{2\sigma}\right)}{|\mathbf{F}|^2} \right). \quad (3.8)$$

3.1.3. Time iterations

By utilizing the obtained gravitational field, the positions and velocities of particles can be updated. This process is carried out in small steps, denoted as dt . The selection of dt is crucial and is determined by the closest pair of particles within the simulation volume. The time step dt governs the position changes through velocity Verlet integration. The velocity Verlet integration for a specific particle at location \mathbf{r} operates as follows, requiring the accelerations at the position of the particles instead of the gravitational field, which can be derived using $\mathbf{a} = \mathbf{g}$:

$$\mathbf{r}_{t+dt} = \mathbf{r}_t + \mathbf{v}_t dt + \frac{1}{2} \mathbf{a}_t dt^2$$

$$\mathbf{v}_{t+dt} = \mathbf{v}_t + \frac{1}{2} (\mathbf{a}_t + \mathbf{a}_{t+dt}) dt$$

velocity Verlet integration offers several significant advantages. Its symplectic nature means that it exactly preserves the symplectic two-form of the phase space, ensuring that the volume in phase space is conserved over time. This property is crucial for the long-term stability of numerical simulations of Hamiltonian systems, where preserving the qualitative behavior of the system is important.

The method achieves second-order accuracy, which means that the local truncation error per step is of the order of $\mathcal{O}(dt^3)$ and the global error is of the order of $\mathcal{O}(dt^2)$. This provides a good balance between computational efficiency and accuracy, as it allows for reasonably large time steps without sacrificing precision.

However, there are also disadvantages. It may not be as accurate for systems where higher-order integration methods are necessary, such as Runge-Kutta integration. Furthermore, the fixed time step dt must be chosen carefully, as too large a time step can lead to instability, while too small a time step can significantly increase computational cost.

3.1.4. Short-range Newtonian correction

A significant limitation of a particle mesh using any kind of smoothing is its inability to accurately determine the gravitational potential and field for particle pairs that are within certain distances from each other. This inaccuracy arises because such particle pairs are unable to approximate each other as point masses and can even have overlapping masses. Because of this, particle mesh is inefficient as it requires all particles to be at least a certain distance apart, necessitating a large grid. Thus, to prevent this inaccuracy and allow for smaller grids, short-range corrections are introduced.

Due to the linearity of accelerations in the Newtonian regime, it is possible to remove the influence of the particle mesh on the acceleration of a particle due to another particle elsewhere. This incorrect acceleration can be removed using the analytical explanation found in Theorem 3.1.3, which is the gravitational field that acts on a particle after interpolation from the grid due to another particle at a certain distance. Hence, the interaction between pairs of particles can be removed whenever they are within a radius r_c where the two particles cannot approximate each other as point masses.

After removing the incorrect accelerations of all pairs of particles with a separation of less than r_c , the correct accelerations need to be added. This is done using Equation (2.5), which represents the acceleration of a point mass due to another point mass. Thus, after the short-range are applied to these particle pairs, their interactions have reduced to direct particle-particle interactions without any effect of the particle mesh, except for the numerical error introduced by the particle mesh.

Finding the distances between all the particles to determine which pairs should use the short-range corrections has a computational complexity of order $\mathcal{O}(n^2)$, with n being the number of particles. This can be reduced to $\mathcal{O}(n \log(n))$ with the use of Tree codes, such as the Barnes-Hut algorithm (Barnes and Hut, 1986). This approach is not implemented, as it is only computationally beneficial when the number of particles exceeds 10000, which will not be the case.

One might also consider applying short-range corrections directly to the potential on the grid itself. Thus, within the same precomputed ball used to place the mass density on the grid, the potential of a pair of particles is first removed using Theorem 2.1.3 and then added using Theorem 2.1.2. After the potential on the grid is corrected, an interpolation step is still required to return to the original particle locations. This method is less accurate than directly correcting the particles' accelerations as a final interpolation is required from the grid to the particles, which cannot be accurate if the potential represents point masses.

One issue with these short-range corrections is that they cannot be used when a MOND effect is present because of the non-linearity in the accelerations. This means that the corrections can only be used when $\mu(\frac{a}{a_0}) \approx 1$. For the standard interpolation function, this is around an acceleration of $7a_0$, which is when the interpolation function is above 0.99. Whenever the acceleration of a particle is above this threshold, the particle will be approximated as fully Newtonian. There will always remain some non-linearity in the accelerations; however, without the use of any short-range corrections the results from the particle mesh are non-physical because of overlapping masses from the Gaussian smoothing.

Softening parameter

Whenever two particles are close to each other, the time steps may be too large to accurately simulate the particle-particle interactions in the short-range corrections. When a pair of particles are close to each other, the change in position in a time step may be of the order of the distance between the two particles. That means that it is possible for two particles to "jump" to an unrealistically close distance,

which causes the force action on the particles to be too high. This leads to instabilities in the simulation and breaks the conservation of total energy. Hence, when calculating the gravitational force with Equation (2.1) a softening parameter ϵ can be introduced to reduce this effect as follows:

$$F_{1,2}(r) = G \frac{M_1 M_2}{r^2 + \epsilon^2}. \quad (3.9)$$

3.2. Calculating the MOND gravitational potential and field

In most cases, the MOND Poisson equation cannot be solved analytically. However, it can be decomposed into a system of coupled linear partial differential equations (Visser et al., 2024):

$$\left\{ \begin{array}{l} \nabla \cdot \mathbf{g}_N = -4\pi G \rho, \quad \nabla \times \mathbf{g}_N = 0, \\ \mathbf{F} = \mathbf{g}_N + \mathbf{H}, \quad \nabla \cdot \mathbf{H} = 0, \\ \mathbf{g}_M = \nu \left(\frac{|\mathbf{F}|}{a_0} \right) \mathbf{F}, \quad \nabla \times \mathbf{g}_M = 0, \\ \mathbf{F} = \mu \left(\frac{|\mathbf{g}_M|}{a_0} \right) \mathbf{g}_M, \end{array} \right. \quad (3.10)$$

In this system, \mathbf{g}_N and \mathbf{g}_M represent the Newtonian and MOND gravitational fields, respectively.

The Newtonian gravitational field is found by using the previously described particle mesh method. Thus, to find the MOND gravitational field, the final step is to solve for \mathbf{H} . This is done using an iterative process by initially assuming $\mathbf{H} = 0$. Then, the MOND gravitational field \mathbf{g}_M can be expressed as:

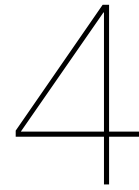
$$\mathbf{g}_M = \nu \left(\frac{|\mathbf{F}|}{a_0} \right) \mathbf{F} = \nu \left(\frac{|\mathbf{F}|}{a_0} \right) \mathbf{g}_N$$

where $\nu \left(\frac{|\mathbf{F}|}{a_0} \right)$ uses the inverse interpolation function, and \mathbf{g}_N is the Newtonian gravitational field.

Next, a new \mathbf{H} can be calculated by first making \mathbf{g}_M curl-free and then using the relation:

$$\mathbf{H} = \mathbf{F} - \mathbf{g}_N = \mu \left(\frac{|\mathbf{g}_M|}{a_0} \right) \mathbf{g}_M - \mathbf{g}_N$$

where $\mu \left(\frac{|\mathbf{g}_M|}{a_0} \right)$ uses the interpolation function. Finally, \mathbf{H} is made rotation-free. For computational efficiency, FFTs are used to make \mathbf{g}_M and \mathbf{H} curl-free and rotation-free, respectively. Iterating this process should allow \mathbf{H} to converge to the correct value (Visser et al., 2024).



Galaxy modelling

4.1. Galaxy models

To simulate a galaxy, one must choose a mathematical model. Starting with a Newtonian potential avoids having to solve for the potential in the Newtonian Poisson equation. To place the particles in the simulation, the mass density function needs to be found by filling in the potential in the Poisson equation. This can lead to extremely long equations for the density if the potential does not have any symmetry. Alternatively, starting with a mass density provides an intuitive understanding of the mass distribution within the galaxy. The drawback of this is that it is not always possible to analytically determine the potential. Thus, beginning with a potential is the simplest approach.

Plummer Model

Before delving into complex galactic models, it is beneficial to start with a simple model to test numerical approaches. The Plummer model (Plummer, 1911) is one such model, used to describe the potential and density distribution of spherical stellar systems such as globular clusters and elliptical galaxies. This model is particularly useful for testing because of its spherical symmetry and starts by defining a Newtonian gravitational potential given by:

$$\Phi_N(r) = -\frac{GM}{\sqrt{r^2 + a^2}},$$

and the corresponding mass probability density function for stellar mass is:

$$\rho(r) = \frac{3a^2}{4\pi(r^2 + a^2)^{5/2}}.$$

The parameter a serves as a scale parameter that determines the core radius of the stellar system. It controls the extent to which the mass density is concentrated toward the center. A smaller a results in a more concentrated central density, while a larger a spreads the density over a larger volume. This parameter ensures a finite central density and a smooth transition of the density profile from the core to the outer regions.

This probability density function comes from the Newtonian Poisson equation. Taking this potential as the MOND potential, and then solving the MOND Poisson equation for the mass probability density function is unnecessary, as we are only required to find a reasonable density function, after which the used Newtonian potential is discarded.

Miyamoto-Nagai Model

Galaxies are often not fully spherical and can even be flat. The Miyamoto-Nagai model Miyamoto and Nagai, 1975 is commonly used (Barros et al., 2016; Granados et al., 2017) to represent the potential

of galactic disks of finite thickness, providing a more realistic approximation of the mass distribution in spiral galaxies. The Newtonian gravitational potential is given in cylindrical coordinates by:

$$\Phi_N(r, z) = -\frac{GM}{\sqrt{r^2 + (\sqrt{z^2 + b^2} + c)^2}},$$

and the corresponding mass probability density function is:

$$\rho(r, z) = \frac{b^2 cr^2 + (c + 3\sqrt{z^2 + b^2})(c + \sqrt{z^2 + b^2})^2}{4\pi [r^2 + (c + \sqrt{z^2 + b^2})^2]^{5/2} (z^2 + b^2)^{3/2}}$$

In the Miyamoto-Nagai model, the parameter b represents the vertical scale height, which defines the thickness of the disk. The parameter c represents the length of the radial scale, which determines the extent of the disk in the radial direction.

4.2. Sampling particle locations

Now that some density profiles are known, the next step is to distribute particles within the simulation volume to perform the simulation. Starting with the probability density functions, a probabilistic method is used to sample the positions of the particles. The resulting mass distribution must match the original probability density function. In the one-dimensional case, the inverse transform sampling is used. However, in the two-dimensional case, additional steps are required to ensure the correct mass distribution.

4.2.1. Inverse transform sampling

Inverse transform sampling uses a probability density function to generate samples of projected radial distances in one dimension. For simplicity, it is assumed that the probability density functions have spherical or circular symmetry, so that spherical or polar coordinates can be used, respectively.

Definition 4.2.1. Let R be a random variable on \mathbb{R}^3 , then the cumulative distribution function of R , $F_R : [0, \infty) \rightarrow [0, 1]$ is defined by:

$$F_R(r) = \mathbb{P}(R \leq r) = \int_{-\infty}^r f_R(x) dx, \quad (4.1)$$

with f_R the probability density function of R .

As a cumulative density function takes in a radial distance r and returns a value in $[0, 1]$, it is possible to invert the cumulative density function to obtain radial distances based on random input $u \in [0, 1]$. In spherical coordinates, it is essential to choose both a polar angle θ and an azimuth angle ϕ . Specifically, θ is sampled from the interval $[0, \pi]$ and ϕ from $[0, 2\pi]$. In contrast, for polar coordinates, the polar angle ϕ is sampled only from the interval $[0, 2\pi]$.

Inverting a cumulative density function can be difficult, especially when a second variable is introduced, and thus needs to be done numerically. Now, let $u \in [0, 1]$, then r can be found by solving equation $F(r) - u = 0$. This is solved using the Newton-Raphson method. This method involves using an initial guess r_0 and then iterating $r_{n+1} = r_n - \frac{F(r_n)}{F'(r_n)}$. The initial value $r_0 = 1$ is chosen as the radii should always be possible.

It is theoretically possible for extremely large r to be sampled such that a particle is outside the simulation volume, requiring the rejection of samples above a certain cutoff radius. Thus, it is important to choose a probability density function that has almost all probability inside the simulation volume to accurately simulate the mass density.

To reduce the high computational cost of using numerical integration and the Newton-Raphson method for every sample, linear interpolation can be used by precomputing a set of radial distances from a set of random values $u \in [0, 1]$.

4.2.2. Multivariate sampling

In cylindrical coordinates, the sampling becomes more difficult as it is necessary to sample both the radial component and the z-component. However, in the mass probability density functions, these two are not separable. Therefore, it is necessary to use marginal probability density functions.

Definition 4.2.2. Let (R, Z) be random variables on $([0, \infty), \mathbb{R}^3)$, and $f_{R,Z}$ the probability density function of (R, Z) , then the marginal probability density function of R is given by:

$$f_R(r) = \int_{-\infty}^{\infty} f_{R,Z}(r, z) dz \quad (4.2)$$

Now, by using inverse transform sampling, the radial distances can be sampled. However, since R and Z depend on each other, it is necessary to sample Z based on a sampled R .

Definition 4.2.3. Let (R, Z) be random variables on $([0, \infty), \mathbb{R}^3)$, and $f_{R,Z}$ the probability density function of (R, Z) , then the probability density function of Z , given R is defined as:

$$f_{Z|R}(r, z) = \frac{f_{R,Z}(r, z)}{f_R(r)} \quad (4.3)$$

So, by inverse transform sampling of the cumulative distribution function of $f_{Z|R}(r, z)$, using a sampled r it is possible to sample a z .

4.2.3. Rejection sampling

Inverse transform sampling can be computationally intensive due to need to compute values for the cumulative density function, which requires integration. Therefore, it might be beneficial to use rejection sampling instead. Like inverse transform sampling, two samplings are performed: one for the radial component and one for the z-component.

For sampling, minimal and maximal values for the radial and z-components need to be chosen. These need to be carefully chosen based on the scale length parameters of the used model. The rejection sampling for the radial component works as follows. Let $r_{max} \in \mathbb{R}$ such that $\mathbb{P}(r > r_{max})$ is negligible. Then sample a value u_1 from a uniform distribution in the interval $[0, r_{max}]$. To reject or accept the value u_1 a proposal distribution is needed. The requirement for this distribution is that it has values always greater than the used probability density function. As a probability density function only has values in $[0, 1]$ a uniform distribution on the same interval is chosen. Now, sample a value u_2 from this new uniform distribution. If $u_2 > f_R(u_1)$, the sample is rejected; otherwise it is accepted. The sampling for the z component is similar, only now u_1 is sampled uniformly from $[z_{min}, z_{max}]$ instead with the requirement that $\mathbb{P}(z \in (-\infty, z_{min}) \cup (z_{max}, \infty))$ is negligible.

Due to the way in which the radial component is sampled in just one dimension, instead of in spherical coordinates, the cumulative density function for the Plummer model in projected radial distances in one dimension is analytically known by Equation (4.4). The real cumulative density function after including the angles in the positions is given by Equation (4.5), where ρ is modified so that the units are correct for spherical coordinates.

$$F(r) = \int_0^r \rho(r') dr' = \frac{3a^2 r + 2r^3}{2(a^2 + r^2)^{3/2}} \quad (4.4)$$

$$F(r) = \int_0^r 4\pi r'^2 \tilde{\rho}(r') dr' \quad (4.5)$$

4.3. Rotation curves

After the positions of the particles are chosen, the initial velocities need to be determined. For both the Plummer and Miyamoto-Nagai models, circular orbits are assumed.

Starting with the Newtonian regime, it is straightforward to analytically calculate an equation for the rotation curve.

Theorem 4.3.1. *The rotation curve equation of a galaxy, assuming circular orbits under Newtonian dynamics, is given by:*

$$v(r) = \sqrt{r a_N(r)}, \quad (4.6)$$

where $v(r)$ is the orbital velocity at a distance r from the galactic center, and $a_N(r)$ is the Newtonian acceleration at that distance.

Proof. Let there be a particle of mass M at a distance r from the galactic center that is centered at the origin of \mathbb{R}^3 . The centripetal force on this particle around the center of mass (the galactic center) is given by:

$$F = M \frac{v^2}{r},$$

where v is the orbital velocity. Rewriting this in terms of acceleration, we get:

$$a_N = \frac{v^2}{r}.$$

Rearranging this equation to solve for v , we obtain Equation (4.6). □

For MOND, finding the rotation curve becomes more challenging because, according to system (3.10), it is necessary to solve for \mathbf{H} to determine the MOND accelerations. However, for simple systems, it is often a reasonable approximation to use $\mathbf{H} = \mathbf{0}$, which is exact for a system of one-dimensional or spherical symmetry (Milgrom, 2010). Thus, the rotation curve equation for circular orbits in MOND can be estimated as follows:

$$v(r) = \sqrt{r a_M(r)} = \sqrt{r a_N v \left(\frac{a_N}{a_0} \right)} \quad (4.7)$$

This approximation, though useful, becomes unusable as the complexity of the model increases. For more complex systems a numerical method is needed. As the velocities are not required until increments of time are involved, the velocities can be determined at $t = 0$ by first calculating the MOND accelerations, and then converting that to an initial velocity for circular orbits. This gives the following relation for the velocity:

$$a_M = v \left(\frac{|\mathbf{F}|}{a_0} \right) F = \frac{v^2}{r} \quad (4.8)$$

5

Testing

5.1. Newtonian particle mesh

Beginning with a purely Newtonian particle mesh, the following numerical methods are tested for their accuracy: I) mass density placement on a grid, II) potential calculation using Fourier transforms, III) transition from potential to gravitational field using the finite central difference and spectral methods, and IV) applying short-range corrections. These methods are evaluated on point masses, Gaussian distributions, and circular and elliptical orbits.

5.1.1. Mass placement

To calculate the gravitational potential using the discrete Fourier transform from Theorem 3.1.2, it is first required to place the mass density of all particles on a grid. For this, a Gaussian distribution of unit variance is used, as is explained in Section 3.1.1. To reduce the computational cost of these mass placements a pre-computed ball of vertex offsets is used. Figure 5.1A shows a smoothed solar mass on a cubic $N = 128$ grid, with the Gaussian distribution centered around the coordinate $(64, 64, 64)$. By visually inspecting Figure 5.1A it appears that a ball with a radius of 3 pixels would suffice; however, as the radius increases, the number of vertices generally increases proportional to the square of the radius. Therefore, even at a radius of 5 pixels there is a significant amount of mass, because a ball of radius 4 can miss up to 0.7% of the total mass for each particle. Figure 5.1B shows the same mass, but shifted by half a pixel in each direction, showing that a larger ball is required.

The reduction in mass in itself is not a problem as it would simply mean that all masses are slightly lower than expected, but would result in accurate orbits for those smaller masses. However, another problem with a ball with a radius of 4 pixels is that it leads to fluctuations in mass depending on where the Gaussian distribution is centered inside a cell. Therefore, a ball with a radius of 5 pixels is more suitable as in the worst case it contains 99.99% of the total mass.

An alternative is to normalize the placed mass inside the ball to the correct value, such that no mass can be lost. This requires summing over and updating each vertex inside the ball, which is about the same computational complexity as increasing the radius from 4 to 5 pixels at the cost of increasing computational complexity.

When interpolating the gravitational field on the grid back to the location of the particles, the same ball and Gaussian is used to maintain consistency, since the same argumentation as above also applies to this interpolation.

Compared to a previous implementation (de Nijs et al., 2023), the computational performance of these placements and interpolations has been significantly increased by using the Python package CuPy (Okuta et al., 2017), which runs these on a GPU. Previously, the computational cost of all FFTs, including the ones required for MOND, was equal to the cost of placing a thousand particles on the grid (Visser et al., 2024). Because the FFTs are independent of the number of particles, the placement of the particles becomes a bottleneck when there are more than a thousand. Now, the computational cost

of placing a thousand masses on a cubic $N = 128$ grid has decreased by a factor of about 75, with both implementations tested for a ball with a radius of 5 pixels. Hence, the computational bottleneck of the simulations in this chapter will be the FFTs.

The computational cost of the FFTs can be reduced with the use of real-to-complex and complex-to-real FFTs, instead of the complex-to-complex FFTs used in this implementation. This should halve the time it takes for each FFT, as in one dimension in k -space the number of pixels can be halved. This feature is not implemented because our simulations did not require this optimization.

Another improvement over the previous implementation is that the mass density no longer has to be placed on a $N \times N \times N$ grid by changing how the \mathbf{k} matrix is generated for the calculation of the Newtonian potential in k -space. This is done by scaling the k -matrix differently in each direction as the spacing in k -space is dependent on the number of pixels in each given direction. This greatly increases performance for the computation of the FFTs where a cubic grid is not required. For example, a $256 \times 256 \times 64$ grid contains only one-quarter of the total number of vertices compared to a $256 \times 256 \times 256$ grid.

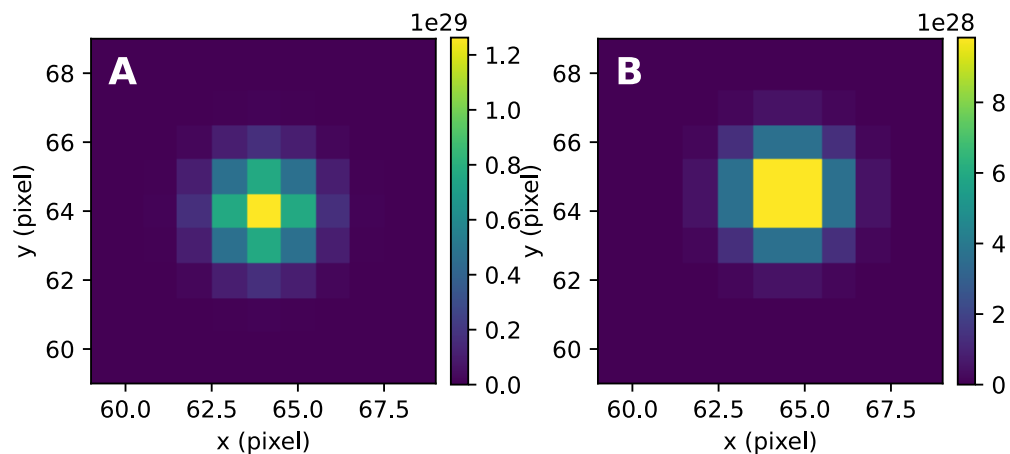


Figure 5.1: A: A 2-dimensional slice of a $128 \times 128 \times 128$ grid on which a single particle of solar mass is placed. The mass is smoothed using a Gaussian distribution, with a variance of 1, centered around the vertex $(64, 64, 64)$. The mass density is plotted for $z = 64$, going through the center of the mass on the xy -plane, and on a logarithmic scale, so that most mass can be easily seen. B: The same smoothed mass, now centered around the coordinate $(64.5, 64.5, 64.5)$.

5.1.2. Gravitational potential and field

Now, using this density grid Theorem 3.1.2 is used to calculate the potential. Figure 5.2 shows the potential of a smoothed solar mass on a cubic $N = 128$ grid with $L = 1$ AU. It also contains the analytical expression for the potential as determined in Theorem 2.1.3. This expression does not seem to match the numerical values at all. This is due to a shift in the potential introduced by the Fourier transforms, which averages the potential to zero. This offset is added to the analytical expression by taking the difference between the lowest numerical and analytical values and then adding that difference to the analytical expression.

The shifted analytical expression visually matches the numerical values, except at the edges of the

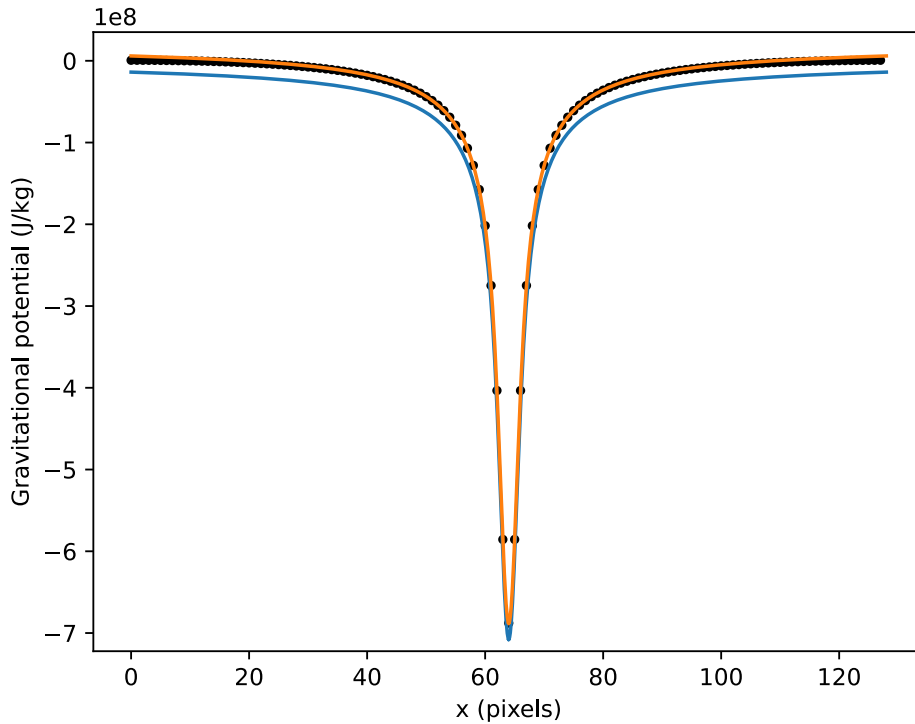


Figure 5.2: The Newtonian potential of a single smoothed solar mass, placed on a $128 \times 128 \times 128$ grid with spacing of 1 AU. The mass is smoothed using a Gaussian distribution with a variance of 1, centered around $(64, 64, 64)$. Due to the spherical symmetry of the potential, only the x direction through the center of the mass is shown. The blue line represents the theoretical Newtonian gravitational potential, and the orange line represents a shifted version, where the bottom corresponds to the lowest numerical value.

grid. This error is introduced by the periodic boundary conditions of the discrete Fourier transform, which create virtual copies in real space that influence the potential at these boundaries. When many particles are involved, this shift may have a significant effect on the potential energy. Without correcting for this shift, it may not be possible to accurately calculate the gravitational potential energy. Thus, when calculating the potential energy, it must be compared with the field energy using Equation (2.23), because the field energy does not include this shift. This shift does not have any effect on the dynamics of the simulation, as calculating the gravitational field eliminates any offset by taking the gradient of the potential.

Before calculating the MOND gravitational field, it is necessary to check the accuracy of its Newtonian counterpart. Figure 5.3A shows the numerical gravitational field, in the x -direction, created by a smoothed mass on a cubic $N = 64$ grid with $L = 1$ AU, centered around the coordinate $(32, 32, 32)$. The corresponding analytical equation from Theorem 2.1.3 is also plotted and visually matches the numerical values.

At distances within a radius of 4 pixels from the center of the mass, the numerical values visually diverge from the Newtonian gravitational field of a point mass. This is caused by the smoothing of the mass density using a ball with a radius of 5 pixels. As this smoothing contains a relatively small amount of matter at the outer edges of the ball, a particle can already be somewhat approximated as a point mass at a distance of 4 pixels. This approximation, while not completely accurate, enables for a much denser packing of particles on the grid without the need for short-range corrections.

Figure 5.3C shows similar results, but now using the central finite difference method instead of the spectral method. To determine which is better, Figures 5.3B/D show the absolute error between the numerical and analytical values for the central finite difference and spectral methods, respectively. The spectral method, compared to the central finite difference method has a smaller absolute error near the

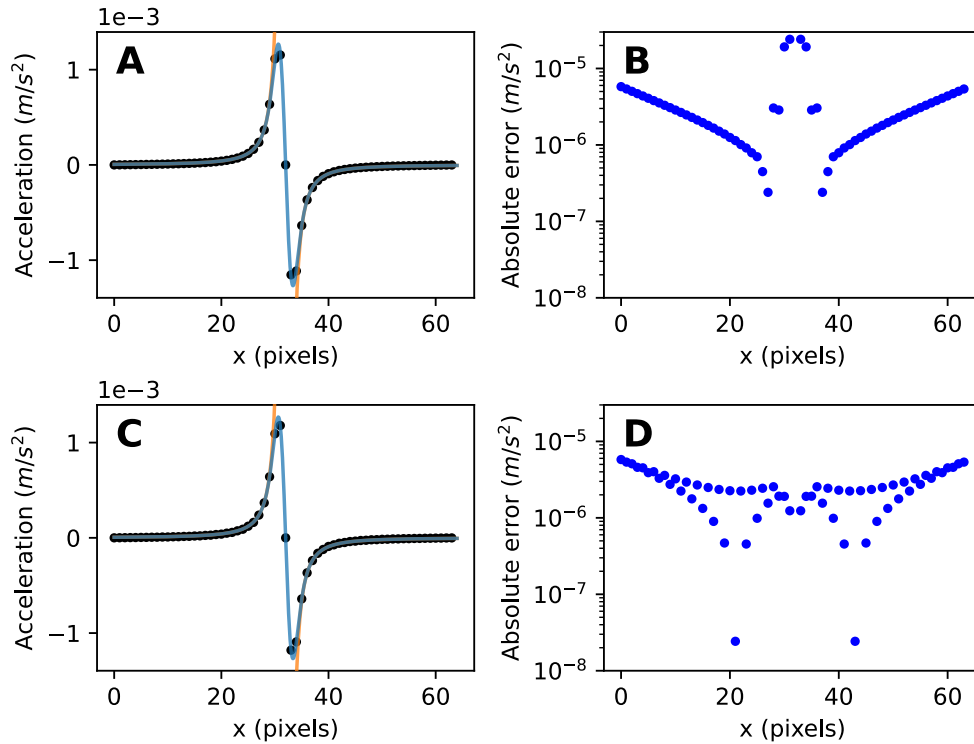


Figure 5.3: A: The Newtonian gravitational field created by a single smoothed solar mass, placed on a $64 \times 64 \times 64$ grid with spacing of 1 AU. The mass is smoothed using a Gaussian distribution with a variance of 1, and centered around $(32, 32, 32)$. Due to spherical symmetry of the gravitational field, only the x direction through the center of the mass is shown. The dots represent the numerically calculated gravitational field using the spectral method for differentiating the Newtonian potential, known only at the vertices. The blue line shows the expected analytical values for a Gaussian smoothing. The orange line is the Newtonian gravitational field of a point mass without smoothing. C: Instead of the spectral method, the central finite difference method is used. B/D: The blue dots represent the absolute error between the numerical and analytical gravitational fields for a Gaussian distribution from figure A and C, respectively.

center of the mass. However, at slightly larger distances from the center, the central finite difference method is better because at these distances it has a significantly smaller absolute error compared to the spectral method.

As the gravitational field rapidly decreases at larger distances from the mass, a large absolute error farther from the mass is relatively more significant than a large absolute error near the mass. Furthermore, at short distances the gravitational field of a point particle is much larger than that of a smoothed mass; thus, after applying the short-range corrections from Section 3.1.4, these absolute errors become relatively less significant. Another downside of the spectral method is that it introduces aliasing effects, whilst the central finite difference method smooths these out. Overall, for these reasons, the central finite difference method is preferred over the spectral method.

5.1.3. Short-range corrections

Now that the Newtonian gravitational field can be accurately determined on the grid, it needs to be interpolated back to the location of the particles using the same Gaussian used to place the mass density on the grid. The expectation is that the interpolated gravitational field matches Theorem 3.1.3, as it represents the interpolated gravitational field acting on a particle due to another mass elsewhere.

Figure 5.4A illustrates the gravitational field acting on a point mass in the x -direction, resulting from a smoothed solar mass located at a certain separation along the same direction. These values are obtained using a cubic $N = 128$ grid, with $L = 1$ AU. The numerical values and the analytical expression of Theorem 3.1.3 visually match. The expected gravitational field for a point mass is also shown and merges with the numerical values at a separation of 5.5 pixels. This implies that a smoothed mass,

using a Gaussian distribution with unit variance, can only be accurately approximated as a point mass at distances greater than 5.5 pixels. Figure 5.4B shows the absolute error between the analytical expression and the numerical values for the interpolated gravitational field. The error is largest at a separation of 0.8 pixels, around 0.8%, and is below 0.2% after a separation of 1.5 pixels.

The significantly higher error at low separations is not an issue. After applying short-range corrections, the gravitational field should align with that of a point particle, which is larger than that of a smoothed mass. This suppresses the relative error as the absolute value of the gravitational field increases, while the error remains unchanged. Figure 5.5A shows this in action. It shows the gravitational field acting on the same two particles, but now the gravitational field after interpolation is corrected using short-range corrections. Figure 5.5B contains the absolute error between the corrected numerical values and the analytical gravitational field for a point mass. The absolute error remained unchanged from that shown in Figure 5.4, which is expected, since the corrections do not significantly affect the error due to the use of an analytical equation. Now, the maximum relative error between the numerical and analytical values decreased from 0.8% without corrections to 0.2% with corrections, while also improving the dynamics of particles in close proximity.

Similar tests were carried out using smaller cubic grids with $N = 64$ and $N = 96$. These tests showed similar results at small separations but higher absolute errors at larger separations. This is because the particles are closer to the edges of the grid, causing virtual copies in real space introduced by the Fourier transforms to have a greater impact.

In general, the results in Figure 5.4 and Figure 5.5 show that the use of short-range corrections is allowed because the analytical expression of Theorem 3.1.3 matches the numerical values, with the relative error between the numerical and analytical expressions decreasing at small separations after corrections compared to before corrections.

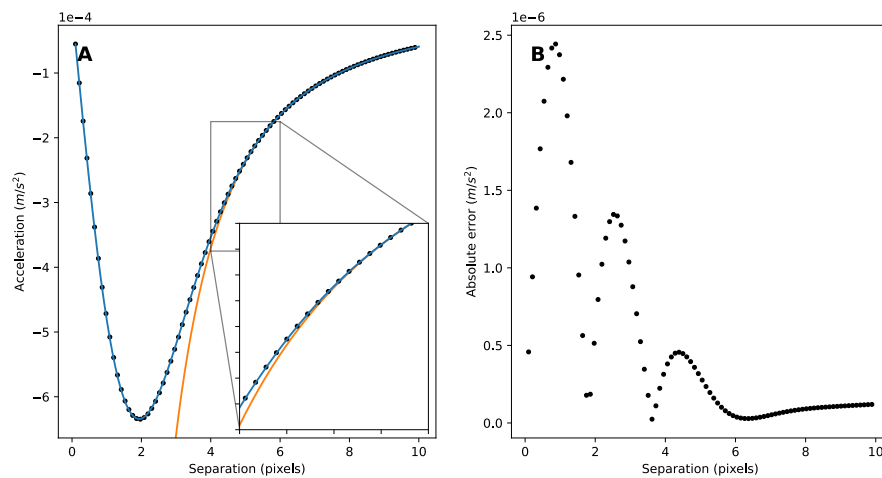


Figure 5.4: A: The gravitational field after interpolation acting on a point mass due to a smoothed solar mass at certain separations. The blue and orange line represents the expected analytical values for the gravitational field due a smoothed and point mass, respectively. These values were obtained using an $128 \times 128 \times 128$ grid, with the edges having a length of 1 AU. B: The absolute error between the numerical values and the analytical expression for a smoothed mass.

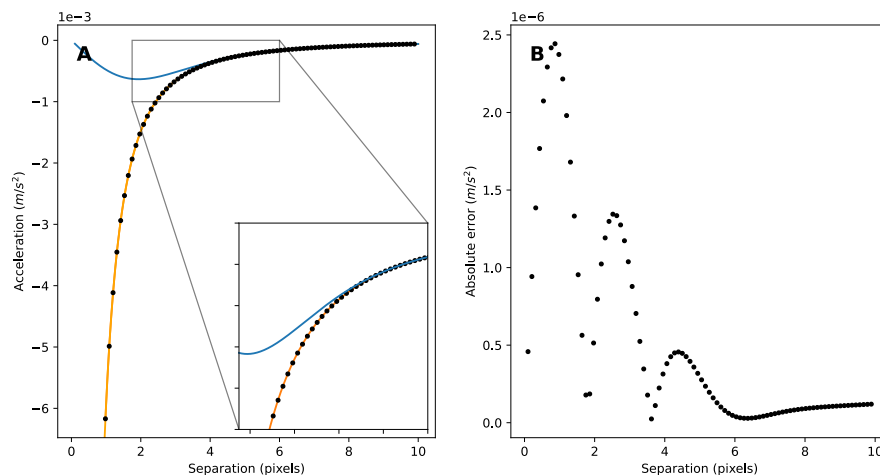


Figure 5.5: The gravitational field after interpolation acting on a point mass due to a smoothed solar mass after the use of short-range corrections at certain separations. The blue and orange line represents the expected analytical values for the gravitational field due a smoothed and point mass, respectively. These values were obtained using an $128 \times 128 \times 128$ grid, with the edges having a length of 1 AU. For visualisation, the first 8 data points have been left out from the graph, but are included in error analysis. B: The absolute error between the numerical values after short-range corrections and the analytical expression for a point mass.

Circular orbits

Since smoothed particles can be fully approximated as point masses at a separation of 5.5 pixels from their center, it is necessary to apply short-range corrections only for pairs of particles with a separation less than that. To reduce the computational cost of these corrections, the separation at which corrections are applied can be reduced at the cost of accuracy.

Figure 5.6A shows two simulations, one with and one without short-range corrections, of two particles in circular orbit around a common center of mass. Their velocities are initialized in the xy -plane, and they are placed at a separation of 2 pixels on a cubic $N = 64$ grid, with $L = 1$ AU. The two simulations ran for 1000 time steps, each representing 3 days. Figure 5.6A, shows that the orbits of the simulation without corrections do not retain their circularity. This is caused by the density smoothing, which does not result in the correct gravitational field at low separations due to overlapping mass density. The orbits in the simulation with short-range corrections retain circularity over time. The maximum deviation from the circular trajectory, approximately 0.4%, occurs when one of the particles reaches the halfway point of its orbit. After this point, the error decreases and the particle returns to its initial position.

Figure 5.6B shows the total, potential, kinetic, and field energies. The relation between the potential and the field energies of Equation (2.23) holds. This indicates that the potential energy is reasonably accurate, despite the shift introduced in the potential by the Fourier transforms. The Virial theorem does not seem to hold. This is because the potential and field energies are calculated for smoothed masses, whereas the Virial theorem is derived from point masses. Both simulations show that the total energy remains constant, with only minor oscillatory behavior caused by numerical errors. The fact that the total energy remains constant without corrections indicates that the velocity Verlet integration works as intended, showcasing its energy-conservation capability. Without short-range corrections, the kinetic, potential, and field energies fluctuate over time, which is not expected for circular orbits. This effect disappears after the use of corrections, which means that the energies show that the orbital dynamics have improved significantly.

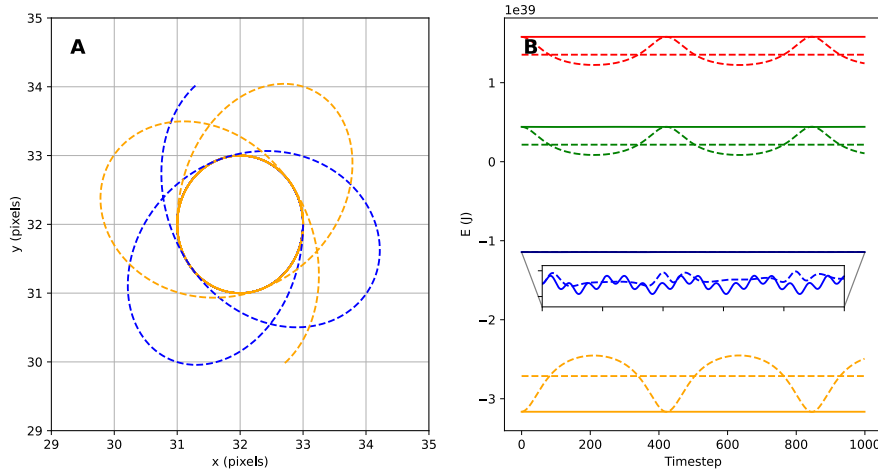


Figure 5.6: A: Two particles placed on a $64 \times 64 \times 64$ grid, with each edge having a length of 1 AU, at an initial separation of 2 pixels. Each particle is initialized with the mass equivalent to one solar mass and an initial velocity for circular orbits around the common center of mass in the xy -plane. The simulation ran for 1000 time steps, each step representing 3 days. The filled and dashed lines represent two different runs, with the dashed lines having no analytical corrections applied while the filled lines do. B: The total, kinetic, potential, and gravitational field energies of the two simulations are shown in blue, green, yellow, and red, respectively. The energies for the simulation without correction also have a straight dashed line plotted through them, representing the average energies.

Elliptical orbits

Not all orbits are circular, they can also be elliptical. Thus, it is necessary to check the accuracy of these kind of orbits, with and without the use of short-range corrections.

Figure 5.7A shows two particles in an elliptical orbit. They are initialized similarly to the circular orbits, but now at $2/5$ -ths the required velocity for circular orbits. The initial separation between the two particles is increased from 2 to 10 pixels to observe the effect when short-range interactions are enabled as the particles approach a distance of 5 pixels and subsequently disabled when they move outside that range. The simulation ran for 1000 time steps, with each time step now representing 2 weeks instead of 3 days. The orbits in the simulation without the use of short-range corrections show that the orbits deviate over time. This is due to the smoothing of the particles that overlap when the particles are within a 5 pixel distance from each other, which results in an inaccurate gravitational field. The use of short-range corrections mostly removes this deviating effect. However, it is not completely removed. This is mainly due to the choice in the size of the time steps. When the two particles are at their nearest, they require a smaller time step compared to when they are farther apart. Decreasing the size of the time steps also decreases the deviation in the orbits. Hence, a balance needs to be made between short-range accuracy and higher computational cost at larger separations.

Figure 5.7B shows the total, kinetic, potential, and field energies of the two simulations. The potential, kinetic, and field energies behave similarly with and without corrections. It shows that the relation between the potential and the field energies of Equation (2.23) also holds for elliptical orbits, indicating that the potential energy is accurate. The difference between the two simulations is visible whenever the two particles are at their nearest, which is when the kinetic energy is at its highest. Here, the kinetic energy is slightly larger with correction compared to that without. This is an expected result, as density smoothing leads to lower velocities due to overlapping mass densities, which cancels a part of the force acting on the particles. Additionally, a significant part of the density is at distances greater than those expected for point masses, resulting in reduced forces, velocities, and kinetic energy. This also explains why the orbits in Figure 5.7A deviate over time is because the velocities are too small whenever the two particles are in close proximity.

For the total energy of the simulation with short-range corrections, Figure 5.7B appears to indicate that it is not maintained properly whenever the two particles are at their nearest. These changes in

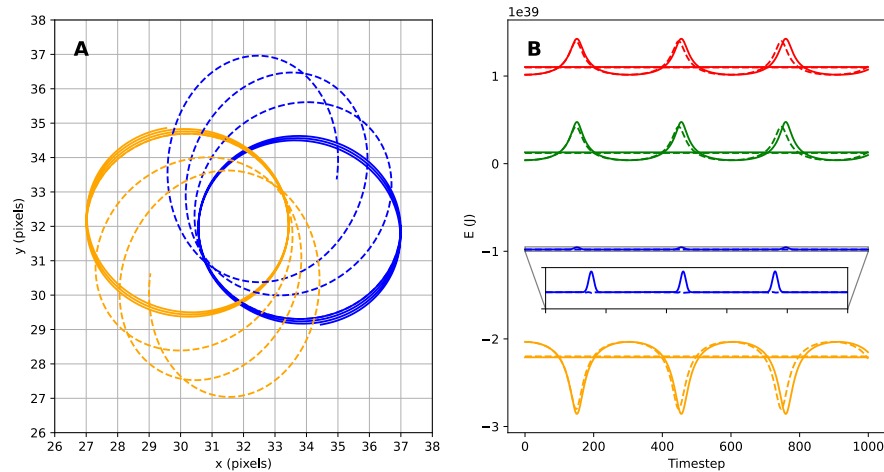


Figure 5.7: A: two particles of solar mass placed on an $64 \times 64 \times 64$ grid, with each edge having a length of 1 AU, at an initial separation of 10 pixels. The velocity of the particles are initialised in the xy-plane at $2/5$ -ths the velocity required for circular orbits around their common center of mass. The simulations ran for 1000 time steps, each representing 2 weeks. The filled lines represent a simulation where analytical corrections are applied, whilst the dashed lines are without. B: The total, potential, kinetic, and field energies are shown in blue, orange, green, and red, respectively. For the last three energies their average energies are plotted as straight lines.

total energy do not come from incorrect orbital mechanics, but come from the fact that the potential and field energies are calculated from the potential grid, without the use of short-range corrections. However, the kinetic energy does contain the effect of short-range corrections as the accelerations, and thus the velocities, of the particles are corrected. When particles move outside a range of 5 pixels, where no corrections are applied, the total energy returns to its original value before corrections are applied.

The kinetic, potential, and field energies show a shift over time when corrections are applied, compared to when they are not. This, in combination with the change in kinetic energy of the energies, shows that the orbital dynamics are significantly influenced by the short-range corrections.

Inaccuracies

Now that the particle mesh can accurately simulate circular and elliptical orbits, there are a few issues that need to be mentioned. If time steps are too small, it becomes computationally expensive to simulate entire orbits. However, if the time steps are too large, the results will be inaccurate because the particles "jump" over each other because the distance traversed in a time step can be too large. In some cases involving a lot of particles, two particles near each other can also jump too closely together. When short-range corrections are applied, this creates an unrealistically high acceleration that shoots these two particles out of the system. This increases the total kinetic energy of the system by too much, breaking the conservation of total energy. A solution to still keep relatively high time steps without fully breaking the conservation of total energy is the introduction of a softening parameter; see Section 3.1.4. This parameter artificially increases the distance between two particles during the application of short-range corrections. This parameter must be set such that it only has a significant influence at really short distances, which are already small when using short-range corrections, and is negligible farther away.

Figure 5.8A shows two particles initialized in the same way as in Figure 5.7, but now with an initial separation and a velocity of 5 pixels and a third the velocity of circular orbits, respectively. The figure shows that the use of a softening parameter, in this case $\epsilon = 0.5$ pixels, turns unstable orbits into stable ones. As the need to use a softening parameter indicates that time steps were too large in the first place, a trade-off must be made between the computational cost of decreasing the size of the time steps and the inaccuracies introduced by time steps that are too large.

Figure 5.8B shows that the energies for the simulation without the use of a softening parameter do

not follow the conservation of the total energy. This is because when the two particles are too close in proximity, they receive an unrealistic acceleration in the short-range correction, which increases the kinetic energy way beyond what should be allowed. With the use of the softening parameter, there are still bumps in the total energy whenever the two particles are at their nearest. This is expected as the kinetic energy is calculated after the application of corrections, whilst the potential and field energies are not.

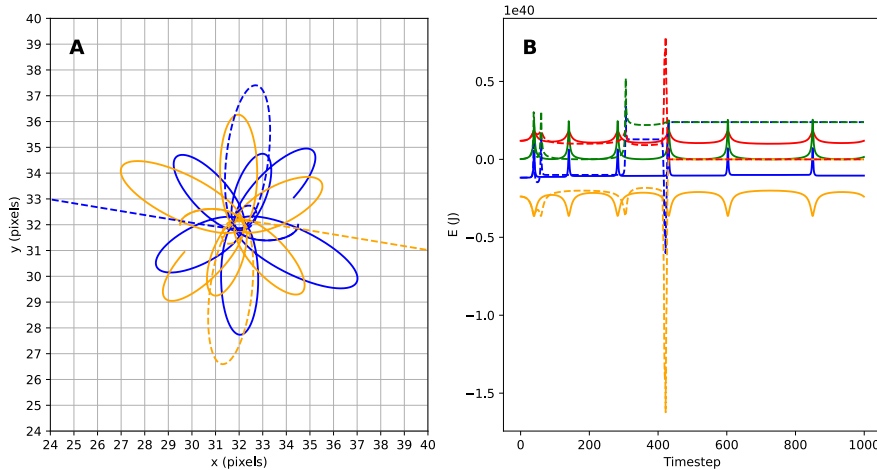


Figure 5.8: A: Two particles of solar mass orbiting each other at an initial velocity of third that for circular orbits. The particles are placed on a $64 \times 64 \times 64$ grid, with each edge having a length of 1 AU. The simulation ran for 1000 time steps, each step representing 2 weeks. The full orange and blue lines are orbits with the use of a softening parameter of $\epsilon = 0.5$ in the analytical corrections. The dashed lines are the orbits without using a softening parameter. B: The total, potential, kinetic and gravitational field energies corresponding to the two simulations colored in blue, orange, green and red, respectively.

5.2. MOND particle mesh

Using the Newtonian gravitational field, the MOND gravitational field is determined using an iterative process, as described in Section 3.2. Figure 5.9A shows the MOND gravitational field of a single smoothed solar mass in deep-MOND on a cubic $N = 128$ grid, with $L = 100000$ AU. The Gaussian distribution of the mass density is centered at $(64, 64, 64)$. For a solar mass, the transition between the Newtonian and deep-MOND regimes starts at around 7000 AU. To find the \mathbf{H} -field, four iteration steps are used, but one iteration often suffices when the spatial steps are small compared to the width of the Gaussian distribution (Visser et al., 2024).

The analytical equation for a smoothed point mass in deep-MOND is known from Corollary 2.2.4 and is plotted together with the numerical values. Figure 5.9B shows the absolute error between the numerical and analytical values. The error increasing near the mass is similar to the Newtonian counterpart in Figure 5.3.

However, now there is a significant oscillatory behavior in the gravitational field and error. These oscillations are introduced by the Fourier transforms used in the iterative process to go from the Newtonian to the MOND gravitational field. To smooth out these oscillations and significantly reduce error at distances greater than 3 pixels, a smoothing is applied using another Fourier transform. By transforming the gravitational field on the grid back to k -space, calculating the potential, and then going back to the gravitational field in real space, the oscillations are effectively removed, which can be seen in Figure 5.9C/D. This comes at the cost of increasing the error near the center of the mass. However, at these distances the gravitational field is inaccurate because of the smoothing of the mass density. Hence, for accurate simulations in deep-MOND no pair of particles may be within a range of 5 pixels anyway. Thus, at the cost of additional Fourier transforms, the error in the gravitational field can be significantly reduced.

For distances near the mass, the absolute error is relatively small compared to the gravitational field

at these distances. However, for larger distances this error is significant, causing a large mismatch between the numerical and analytical values. This mismatch arises because the MOND potential does not approach zero as the distance increases to infinity; instead, it behaves like a logarithm, which continues to increase indefinitely. Consequently, due to the periodic boundary conditions of the discrete Fourier transforms, the copies of the particle have a greater impact on the MOND potential than they would have in the Newtonian case. Testing showed that, due to this behavior, in extreme cases, at most the inner $\frac{2N_x}{3} \times \frac{2N_y}{3} \times \frac{2N_z}{3}$ of the grid can be used in the MOND particle mesh.

Due to not being able to apply short-distance corrections in MOND, a wide binary system from (Visser et al., 2024) is used to determine the closest particles can be before the particle mesh returns non-physical results. Figure 5.10A shows two particles in the wide binary in deep-MOND with a mass ratio of 3 : 2, with the outer mass having the largest mass, and the smaller being one solar mass. The particles are placed on a cubic $N = 64$ grid and initialized at a 2.5 pixel separation, with $L = 100000$ AU. The simulation ran for 1000 time steps, each representing 80000 years. The figure shows that the orbits remain stable at this separation, even though they are not perfectly circular. Reducing the separation below 2.5 pixels causes the orbits to significantly lose their circular shape. Thus, when modeling particles for which corrections cannot be applied, it is important to check whether the particles are at least 2.5 pixels apart, whilst keeping them far away from the edges of the grid.

When particles are neither fully in the Newtonian or deep-MOND regimes, the interpolation function determines the transition between these two regimes. Figure 5.11A shows the gravitational field under the standard interpolation function of a smoothed solar mass. The particle is placed at coordinate (64, 64, 64) on a cubic $N = 128$ grid. The figure also contains the analytical expression derived in Corollary 2.2.2, together with the analytical expressions for the Newtonian and deep-MOND regimes. To see the transition between the two regimes, $L = 1000$ AU is used. That means that the gravitational field of the particle should start to transition from the Newtonian to the deep-MOND regime at a distance of around 7 pixels. Indeed, Figure 5.11A shows that the numerical results clearly diverge from the Newtonian gravitational field at a distance of about 6 pixels and are clearly in the deep-MOND regime after 20 pixels. Figure 5.11B shows the absolute error between the analytical and numerical values and behaves similar to the absolute error of a particle in deep MOND.

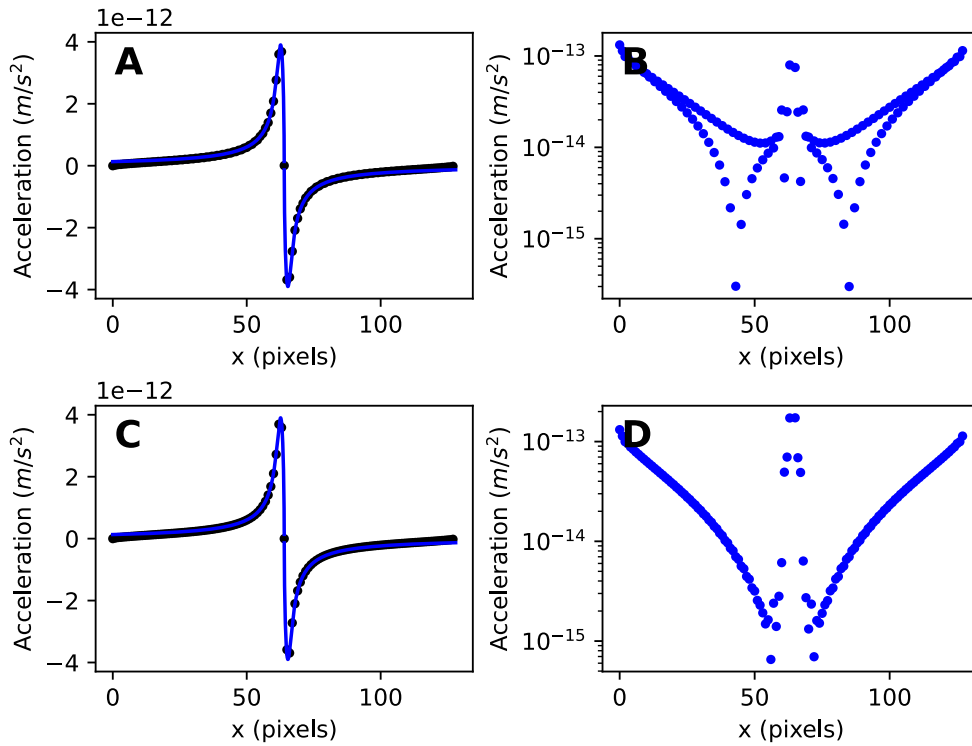


Figure 5.9: A: The gravitational field of a smoothed point particle with solar mass on a $128 \times 128 \times 128$ grid, centered at coordinate (64, 64, 64). The edges of the pixels have a length of 100000 AU, ensuring the shown gravitational field is that of deep-MOND. Through the numerical values, black dots, an analytical solution is plotted, blue line. B: The absolute error between the numerical and analytical values.

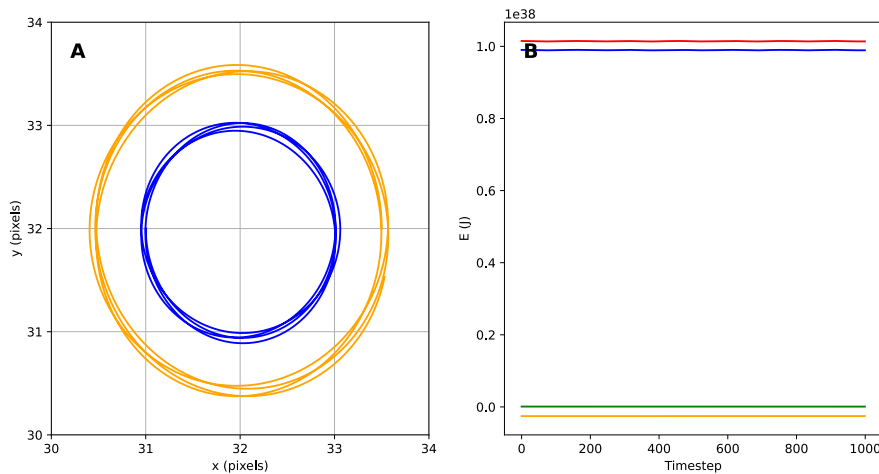


Figure 5.10: A: Two particles with a mass ratio of 3 : 2, with the lower being one solar mass, in deep-MOND on an $64 \times 64 \times 64$ grid, with each edge having a length of 100000 AU. The particles are initialised such that they should always remain at a separation of 2.5 pixels, with the outer particle having the most mass of the two. The simulation ran for 1000 time steps, each step representing 80000 years. B: The corresponding total, potential, kinetic and gravitational field energies, colored in blue, orange, green and red, respectively.

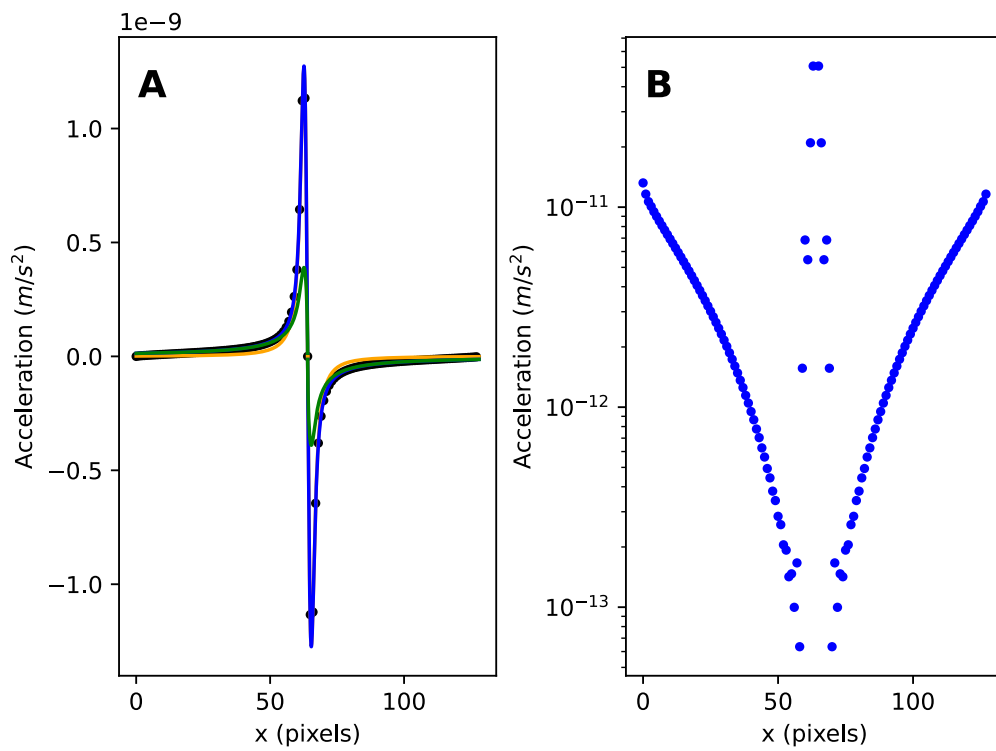


Figure 5.11: A: The MOND gravitational field, using the standard interpolation function, of a smoothed solar mass on a $128 \times 128 \times 128$ grid, centered around $(64, 64, 64)$. The edges of the pixels have a length of 1000 AU, such that both Newtonian and deep-MOND effects are expected. The analytical expressions for the Newtonian, deep-MOND, and standard interpolation function gravitational field are shown in orange, green, and blue, respectively. B: The absolute error between the numerical values and the analytical expression using the standard interpolation function.

5.3. Galactic simulations

5.3.1. Probabilistic sampling

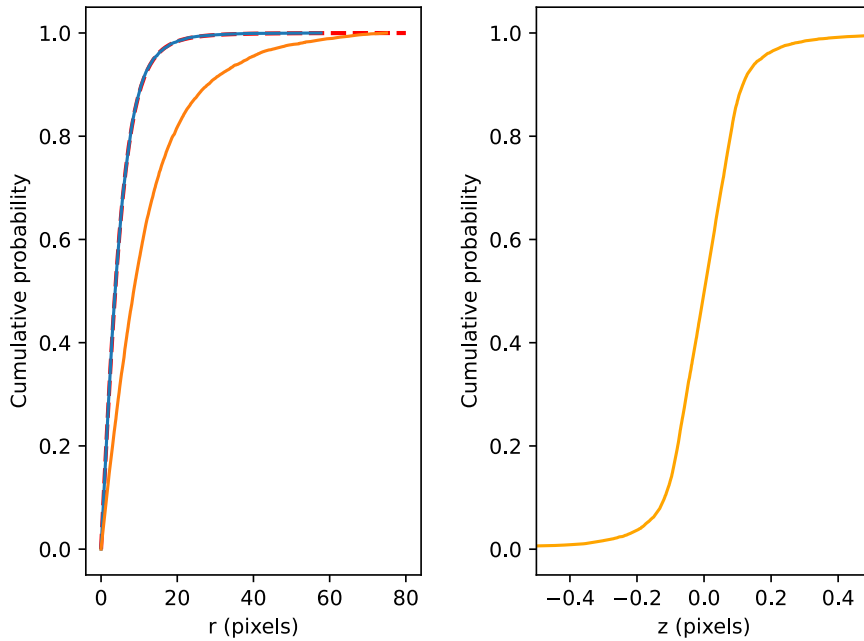


Figure 5.12: The Plummer, and Miyamoto-Nagai mass density functions sampled 10000 times using the rejection sampling method. The Plummer model, the solid blue line, uses a scale length of $a = 10$ pixels. Using this same scale length, the analytically known expression for the cumulative density function of the Plummer model is plotted as a dashed red line. The Miyamoto-nagai, the orange solid lines, model uses the scale lengths $b = 15$, and $c = 0.04$ pixels for the radial and z-components, respectively.

To simulate a galactic disk or sphere, particle locations are sampled. The Plummer and Miyamoto-Nagai models are used to simulate a sphere and disk, respectively. Both are sampled using the rejection sampling method. The inverse transform sampling method was also tested and gave similar results at a much larger computational cost. This is due to the extra steps that involve the numerical computation of integrals and the use of the Newton-Raphson method to find the inverse cumulative density function, which rejection sampling does not require.

Figure 5.12 shows the cumulative probability for the radial component of the bulge, and the radial and z-component of the disk. Both are sampled 10000 times to check for unexpected behavior. The sphere's scale length is set to $a = 10$, resulting in a sphere with an approximate radius of 20 pixels. Consequently, the sphere's diameter is 40 pixels, allowing it to fit comfortably within a cubic $N = 96$ grid, keeping particles well away from the grid's edges. For the disk, scale lengths of $b = 15$ and $c = 0.04$ are used. This disk has a radius of 70 pixels and a thickness of 0.4 pixels, fitting well within a $192 \times 192 \times 64$ grid.

For the sphere, the analytically known cumulative density function of Equation (4.4) is also shown. Note that the radial component is sampled before assigning angles and is thus compared to the analytical equation for the projected radial sampling in one dimension. That the analytical equation and the sampled cumulative probability match indicate that the rejection sampling works as expected.

5.3.2. Plummer model

To simulate the Plummer model, a cubic $N = 96$ grid is used. Instead of the 10000 samples used to test the rejection sampling, in this simulation only 400 particles are used. This number of particles is chosen to ensure that there is enough separation between the particles when using MOND.

The downside of the short-range corrections is that they may only be applied when the acceleration

of the particles can be approximated as fully Newtonian. That is, the interpolation function close to 1. For this simulation, the standard interpolation function is used. This means that to use short-range corrections, L must be chosen such that the particles near the center of the galaxy are fully Newtonian. This is also helped by the use of an additional mass placed at the center of the galaxy, which represents a black hole containing 25% of the total mass. Then, surrounding this central mass, all particles within a radius of 1 pixel are removed to prevent instability directly after starting the simulation, as seen in Figure 5.8. This reduced the total number of particles to 352. To further prevent instability over time due to the use of large time steps, a softening parameter of $\epsilon = 0.05$ pixels is used. The need for these adjustments can be prevented by introducing adaptive time-stepping, meaning that whenever two particles are close to each other, they are simulated using smaller and more time steps. This significantly complicates the simulation, and that is why this approach is not implemented.

Figure 5.13 shows the behavior of the interpolation function in the first time step when $L = 0.7$ kpc and at a total mass of 200 billion solar masses. Short-range corrections are only used for particles for which the interpolation function is above a 0.99 threshold, so that they can be approximated as fully Newtonian and if there are any other particles within a 5 pixel radius.

Now, it is important to check whether most of the pairs of particles for which no correction is applied have a separation of at least 2.5 pixels, so that the orbits remain somewhat accurate as in Figure 5.10. This can be seen in Figure 5.14, which shows these separations in the first time step. There are some pairs of particles for which the separation is less than 2.5 pixels, but the number of pairs for which this is the case is small. This could have been avoided by adjusting the way the angles are chosen when sampling so that when a pair of particles is outside the Newtonian regime and has a separation less than 2.5 pixels, new angles are selected. However, this adjustment comes at the cost of further deviating from the Plummer model, which is why this is not implemented.

Under these conditions, the simulation was run four times: twice fully Newtonian, one with and one without short-range corrections; and twice using MOND, again with and without corrections. Figure 5.15A shows the energies for the Newtonian simulations, which ran for 2000 time steps, each representing 12500 years. The simulation without corrections shows that the total energy is stable. However, the potential and field energies seem to increase and decrease over time. This indicates that the sphere is not fully stable, spreading out, and then retracting over time, which is unexpected behavior, as the sphere should remain stable. This effect is reduced in the simulations with corrections. Both simulations show that the relation between the potential and field energies of Equation (2.23) holds, which is expected for Newtonian simulations. This indicates a significant improvement in the orbital dynamics of the particles.

However, the simulation with corrections shows that the total energy is not constant over time. This is primarily caused by the instabilities seen in Figure 5.8, even after emptying a 1 pixel radius from the central mass and using a softening parameter. These instabilities cause an unrealistic increase in the velocities and thus kinetic energy over time, which also increases the total energy.

Figure 5.15B shows the results using MOND, again with and without the use of short-range corrections. The simulation without corrections is very similar to its Newtonian counterpart. The only difference is that the relation between the potential and field energies no longer holds. This shows that there is a significant MOND effect in the simulation. Again, the simulation with corrections shows that the kinetic, potential, and field energies are much flatter, indicating that the sphere is more stable with than without the use of short-range corrections.

Although some limitations were necessary to simulate the Plummer model, the results indicate that under these conditions, the use of short-range corrections led to more stable and presumably more physical outcomes compared to simulations without these corrections.

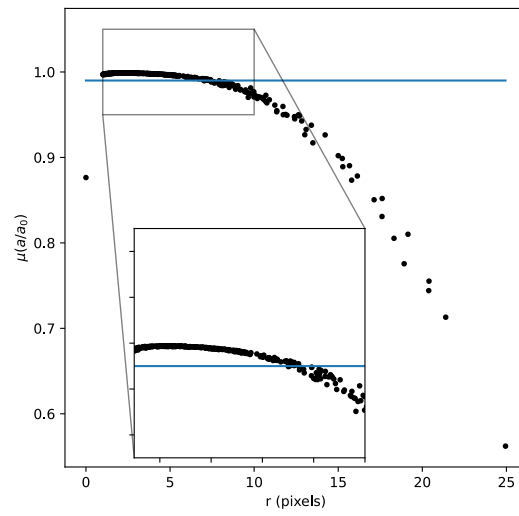


Figure 5.13: The values of the standard interpolation for the Plummer model, with a blue line to indicate the 0.99 threshold.

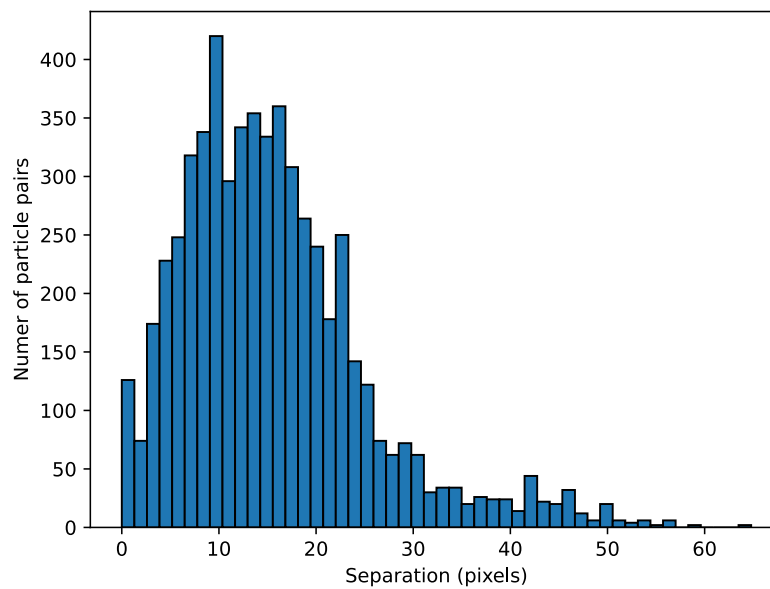


Figure 5.14: A histogram of the separation between all pairs of particles in the Plummer model for which no short-range corrections are applied.

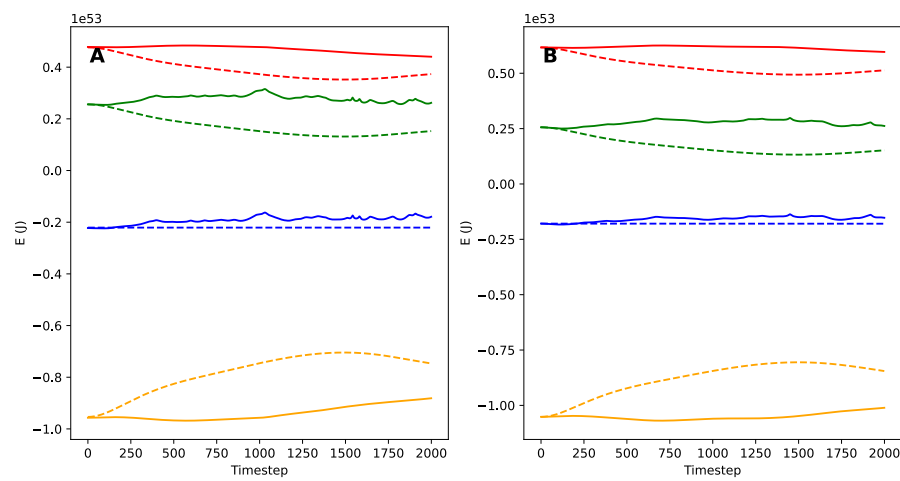


Figure 5.15: A: The energies of Newtonian simulations of a galactic sphere using the Plummer model. The sphere is initialised with 400 particles, each having a mass of 375 million solar masses. A stabilising mass is added at the center of the disk, with a mass of 50 billion solar masses, which is 25% of the total mass. The particles are placed on a $96 \times 96 \times 96$ grid, with each edge having a length of 0.7 kpc. The simulation is run twice: once with analytical corrections and once without. The filled lines represent the simulation with analytical corrections, while the dashed lines represent the simulation without. Each simulation is consists of 1000 time steps, each representing 12500 years. B: The same simulations, but now using MOND, with again the filled and dashed lines representing a simulation with and without the use of corrections, respectively.

5.3.3. Miyamoto-Nagai model

The Miyamoto-Nagai model is simulated similarly to the Plummer model, but now on a $192 \times 192 \times 64$ grid, with $L = 0.45$ kpc. The removal of particles within a radius of 1 pixels from the center reduced their number from 400 to 371. Under these conditions, Figure 5.16 shows the behavior of the interpolation function. Now, compared to the Plummer model, there is a significant increase in the particle for which no corrections may be applied.

Placing the particles such that most pairs of particles are at a separation of 2.5 pixels whenever no short-range corrections are applied is difficult. This can be seen in Figure 5.17, where many pairs of particles have a separation of less than 2.5 pixels. This means that for those pairs the simulation is inaccurate. This could have been somewhat L , such that more particles can be approximated as fully Newtonian. However, due to the shape of the disk, there will remain a significant amount of particle pairs within a separation of 2.5 pixels as the histogram in Figure 5.17 shifts to the left.

Figure 5.18A shows the results for the Newtonian simulations. The total energy without short-range corrections remains constant, with the same effect in the gravitational potential and field energies as in the Plummer model. This indicates that the radius of the disk first increases and then decreases, which is nonphysical behavior. With the use of short-range corrections, this behavior is significantly reduced, as is desired.

Figure 5.18B shows the simulations using MOND. Now, there is an unexpected result. The total energy seems to increase with time, even without the use of short-range corrections. This indicates that some energy is leaking into the system. The most likely cause of this is due to the choice in the number of pixels in the z -direction, which potentially leads to influence of copies in real space due to the periodicity of the discrete Fourier transforms. However, increasing the number of pixels significantly increases the computational cost of the simulation, which seems impossible to prevent in this case. The simulation with short-range corrections shows a similar trend, but should still lead to a more physical result due to the increase in accuracy of the orbits near the center of the disk.

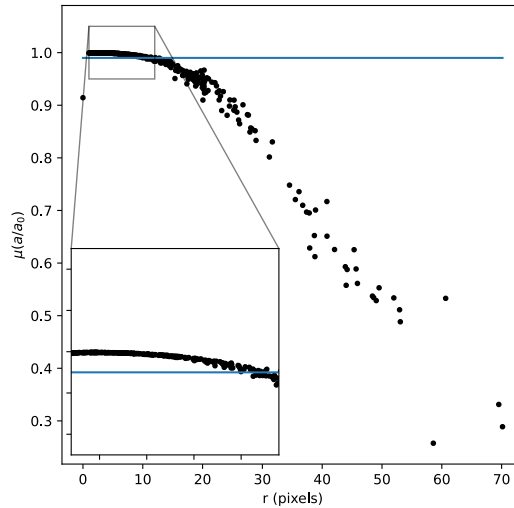


Figure 5.16: The values of the standard interpolation for the Miyamoto-Nagai model, with a blue line to indicate the 0.99 threshold.

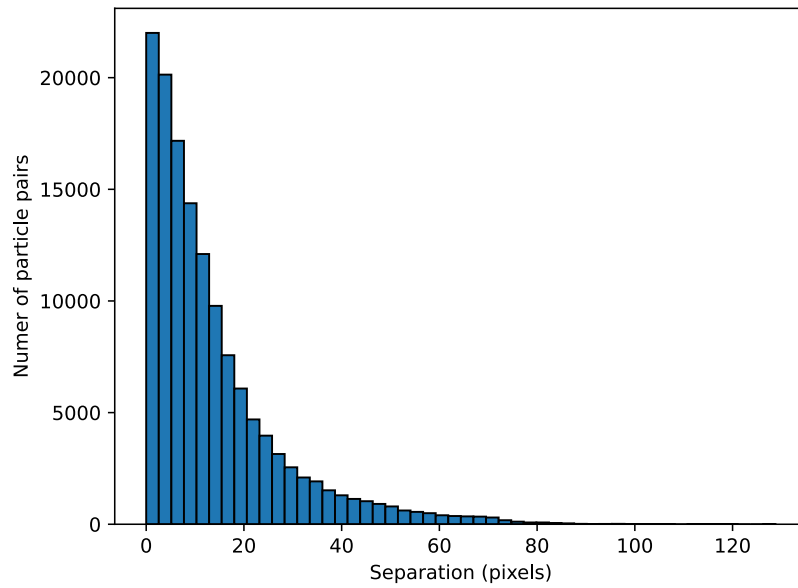


Figure 5.17: A histogram of the separation between all pairs of particles in the Miyamoto-Nagai model for which no short-range corrections are applied.

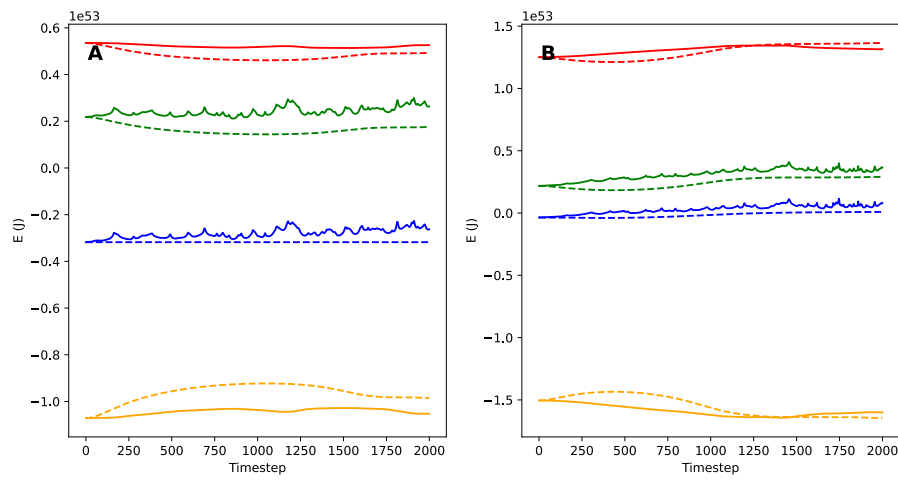


Figure 5.18: A: The energies of Newtonian simulations of a galactic disk using the Miyamoto-Nagai model. The disk is initialised with 400 particles, each having a mass of 375 million solar masses. A stabilising mass is added at the center of the disk, with a mass of 50 billion solar masses, which is 25% of the total mass. The particles are placed on a $192 \times 192 \times 32$ grid, with each edge having a length of 0.45 kpc. The simulation is run twice: once with analytical corrections and once without. The filled lines represent the simulation with analytical corrections, while the dashed lines represent the simulation without. Each simulation consists of 1000 time steps, each representing 12500 years. B: The same simulations, but now using MOND, with again the filled and dashed lines representing a simulation with and without the use of corrections, respectively.



Conclusions and Research Recommendations

6.1. Conclusions

This paper has introduced several methods to increase the accuracy of the particle mesh method for both Newtonian and modified Newtonian dynamics.

Firstly, the mass density is placed onto the grid using a pre-computed vertex ball with a radius of 5 pixels. Using a GPU, a 75-fold improvement in speed is achieved for mass placement onto the grid.

Secondly, the fourth-order central finite-difference method is used instead of the spectral method. This approach demonstrated less error farther away from a mass compared to the spectral method. This reduction in error is desirable because, after short-range corrections, the error near the mass becomes relatively less significant than the error farther away.

Then, short-range corrections are applied to correct the accelerations of particles in the Newtonian regime. This is necessary because when two particles are in close proximity, they cannot approximate each other as point masses due to the overlapping mass density introduced by Gaussian smoothing.

These corrections are first tested by placing two particles at a certain separation and calculating the gravitational field acting on one of them. The correction proves successful, as the maximum error between analytical and numerical values is at most 0.2%.

For two particles in circular orbit with a separation of 2 pixels, the maximum error in their orbit is only 0.4% after short-range corrections are applied. Without these corrections, the orbits of the two particles are not circular, as can also be seen in the oscillations of their kinetic, potential, and field energies. With and without short-range corrections, the total energy remains constant with minimal numerical error. Thus, the use of short-range corrections is effective in improving the orbital dynamics of circular orbits.

For elliptical orbits, short-range corrections also result in a significant improvement. However, when two particles get too close to each other, the choice of time steps must be based on their nearest approach to prevent large errors. This can lead to very small time steps, significantly increasing the computational cost of simulating orbits. To address this, a softening parameter is introduced and tested to increase the length of the time steps at the cost of some accuracy. This parameter allows for larger time steps, stabilizing unstable orbits, and improving the conservation of total energy.

In MOND, short-range corrections can only be used when both particles are fully in the Newtonian regime. The accuracy between particles in MOND needs to be tested for low separations. For this, two particles are placed into circular orbits in deep-MOND at a separation of 2.5 pixels. The orbits remain

visually circular but lose their circularity as this distance decreases. Thus, in MOND, it is crucial that the separation between particles is at least 2.5 pixels.

Finally, the short-range corrections are tested with multiple particles using the Plummer and Miyamoto-Nagai models for a spherical and a disk galaxy, respectively. The simulations for the Plummer model are successful; after short-range corrections, the potential, kinetic, and field energies change less over time compared to simulations without corrections, indicating more stable orbits of particles inside the sphere. The simulation for the Miyamoto-Nagai model is less successful because of how the particles were initialized. Too many pairs of particles remain too close to each other at accelerations where no short-range corrections may be applied, which is a significant limitation in MOND. This leads to inaccurate results as a result of overlapping mass. Another issue is the increase in total energy over time, both with and without corrections, indicating energy leakage into the system. This could be mitigated by increasing the number of pixels, albeit at a significant computational cost.

6.2. Research recommendations

Now that it is possible to increase the accuracy of orbits for galaxies in both Newtonian and modified Newtonian dynamics, there are many ways in which short-range corrections can be utilized. These include, but are not limited to, globular clusters, dwarf galaxies, elliptical galaxies, and galaxy collisions.

However, many improvements remain to be implemented to further increase computational efficiency and accuracy. One way to decrease the computational cost of FFTs is the use of complex-to-real and real-to-complex FFTs, which halves the computational cost by reducing the number of pixels in one dimension by half in k -space.

To increase the accuracy of particle pairs that are too close to each other at a given time step size, adaptive time-stepping can remove the need for a softening parameter. This method decreases the time step size and increases the number of time steps used whenever two particles are near each other.

When using short-range corrections, it is required to calculate the distance between all particles. This has a computational complexity of $\mathcal{O}(n^2)$. This can be reduced to $\mathcal{O}(n \log(n))$ using tree code, such as the Barnes-Hut algorithm (Barnes and Hut, 1986), to determine which particles are close to each other.

Additionally, it might be possible to change the way Gaussian smoothing is used for close encounters. When two particles are near each other, modifying the variance of the Gaussian distribution could aid in approximating the particles as point masses.

Bibliography

- Arbey, A., & Mahmoudi, F. (2021). Dark matter and the early universe: A review. *Progress in Particle and Nuclear Physics*, 119. <https://doi.org/10.1016/j.pnnp.2021.103865>
- Barnes, J., & Hut, P. (1986). A hierarchical $O(N \log N)$ force-calculation algorithm. *Nature*, 324(6096), 446–449. <https://doi.org/10.1038/324446a0>
- Barnett, A. H., Magland, J., & af Klinteberg, L. (2019). A parallel nonuniform fast fourier transform library based on an “exponential of semicircle” kernel. *SIAM Journal on Scientific Computing*, 41(5), C479–C504. <https://doi.org/10.1137/18m120885x>
- Barros, D. A., Lépine, J. R. D., & Dias, W. S. (2016). Models for the 3d axisymmetric gravitational potential of the milky way galaxy. *Astronomy and Astrophysics*, 593. <https://doi.org/10.1051/0004-6361/201527535>
- Cooley, J. W., & Tukey, J. W. (1965). An algorithm for the machine calculation of complex fourier series. *Mathematics of Computation*, 19(90). <https://doi.org/10.2307/2003354>
- Darden, T., York, D., & Pedersen, L. (1993). Particle mesh ewald: An $O(N^2)$ method for ewald sums in large systems. *The Journal of Chemical Physics*, 98(12), 10089–10092. <https://doi.org/10.1063/1.464397>
- de Blok, W. J. G. (2010). The core-cusp problem. *Advances in Astronomy*, 2010, 1–14. <https://doi.org/10.1155/2010/789293>
- de Nijs, J. V., Visser, P. M., & Eijt, S. W. H. (2023). Mondpmesh: Particle-mesh code for milgromian dynamics. *Astrophysics Source Code Library, record ascl:2311.006*.
- Famaey, B., & Binney, J. (2005). Modified newtonian dynamics in the milky way. *Monthly Notices of the Royal Astronomical Society*, 363(2), 603–608. <https://doi.org/10.1111/j.1365-2966.2005.09474.x>
- Gentile, G., Famaey, B., & de Blok, W. J. G. (2011). Things about mond. *Astronomy and Astrophysics*, 527. <https://doi.org/10.1051/0004-6361/201015283>
- Granados, A., Henaó, L., Vanegas, S., & Castaneda, L. (2017). Galrotpy: An educational tool to understand and parametrize the rotation curve and gravitational potential of disk-like galaxies.
- Hockney, R. W., & Eastwood, J. W. (1988). *Computer simulation using particles*.
- McGaugh, S. (2008). Milky way mass models and mond. *The Astrophysical Journal*, 683(1), 137–148. <https://doi.org/10.1086/589148>
- Milgrom, M. (1983a). A modification of the newtonian dynamics - implications for galaxies. *The Astrophysical Journal*, 270. <https://doi.org/10.1086/161131>
- Milgrom, M. (1983b). A modification of the newtonian dynamics as a possible alternative to the hidden mass hypothesis. *The Astrophysical Journal*, 270. <https://doi.org/10.1086/161130>
- Milgrom, M. (2010). Quasi-linear formulation of mond. *Monthly Notices of the Royal Astronomical Society*, 403(2), 886–895. <https://doi.org/10.1111/j.1365-2966.2009.16184.x>
- Milgrom, M. (2023). Generalizations of quasilinear mond. *Physical Review D*, 108(8). <https://doi.org/10.1103/PhysRevD.108.084005>
- Milgrom, M., & Sanders, R. H. (2008). Rings and shells of “dark matter” as mond artifacts. *The Astrophysical Journal*, 678(1), 131–143. <https://doi.org/10.1086/529119>
- Miyamoto, M., & Nagai, R. (1975). Three-dimensional models for the distribution of mass in galaxies. *Publications of the Astronomical Society of Japan*, 27, 533–543.
- Newton, I. (1687). *Philosophiæ Naturalis Principia Mathematica*. <https://doi.org/10.3931/e-rara-440>
- Okuta, R., Unno, Y., Nishino, D., Hido, S., & Loomis, C. (2017). Cupy: A numpy-compatible library for nvidia gpu calculations. *Proceedings of Workshop on Machine Learning Systems (LearningSys) in The Thirty-first Annual Conference on Neural Information Processing Systems (NIPS)*. http://learningsys.org/nips17/assets/papers/paper_16.pdf
- Perivolaropoulos, L., & Skara, F. (2022). Challenges for Λ CDM: An update. *New Astronomy Reviews*, 95. <https://doi.org/10.1016/j.newar.2022.101659>

- Persic, M., Salucci, P., & Stel, F. (1996). Erratum: The universal rotation curve of spiral galaxies – i. the dark matter connection. *Monthly Notices of the Royal Astronomical Society*, 283(3), 1102–1102. <https://doi.org/10.1093/mnras/283.3.1102>
- Plummer, H. C. (1911). On the problem of distribution in globular star clusters: (plate 8.) *Monthly Notices of the Royal Astronomical Society*, 71(5), 460–470. <https://doi.org/10.1093/mnras/71.5.460>
- Visser, P. M., Eijt, S. W. H., & de Nijs, J. V. (2024). Fast particle-mesh code for milgromian dynamics. *Astronomy and Astrophysics*, 681. <https://doi.org/10.1051/0004-6361/202347830>
- Yao, Y., & Capecelatro, J. (2021). An accurate particle-mesh method for simulating charged particles in wall-bounded flows. *Powder Technology*, 387, 239–250. <https://doi.org/10.1016/j.powtec.2021.04.012>
- Yfantis, E. A., & Borgman, L. E. (1981). Fast fourier transforms 2-3-5. *Computers and Geosciences*, 7(1), 99–108. [https://doi.org/10.1016/0098-3004\(81\)90041-8](https://doi.org/10.1016/0098-3004(81)90041-8)
- Zhao, H. S., & Famaey, B. (2006). Refining the mond interpolating function and teves lagrangian. *The Astrophysical Journal*, 638(1), L9–L12. <https://doi.org/10.1086/500805>